

Fermi Large Area Telescope Fourth Source Catalog

THE *Fermi*-LAT COLLABORATION

ABSTRACT

We distribute a preliminary version of the fourth *Fermi* Large Area Telescope source catalog (4FGL) meant to help in writing 2019 NASA *Fermi* Guest Investigator proposals. This supersedes the FL8Y source list distributed in 2018^{a)}.

Based on the first eight years of science data from the *Fermi* Gamma-ray Space Telescope mission and the 50 MeV–1 TeV range, it is the deepest yet in this energy range. Relative to the 3FGL catalog, the 4FGL catalog has twice as much exposure as well as a number of analysis improvements, including an updated model for Galactic diffuse γ -ray emission. The 4FGL catalog includes 5098 sources above 4σ significance, for which we provide localization and spectral properties. Seventy-five sources are modeled explicitly as spatially extended, and overall 357 sources are considered as identified based on angular extent or correlated variability observed at other wavelengths. For 1525 sources we have not found plausible counterparts at other wavelengths. More than 2940 of the identified or associated sources are active galaxies of the blazar class, 241 are pulsars.

Keywords: Gamma rays: general — surveys — catalogs

1. INTRODUCTION

This document presents the fourth catalog of high-energy γ -ray sources (4FGL) detected in the first eight years of the *Fermi* Gamma-ray Space Telescope mission by the Large Area Telescope (LAT). The list is final and this version contains all the source information usually released in Fermi catalogs except for the spectral energy distributions in broad bins, the light curves and several flags. A detailed comparison with previous *Fermi*-LAT catalogs and the careful assessment of c sources are also deferred to a future release. As in the Third LAT Source Catalog (hereafter 3FGL, Acero et al. 2015) sources are included based on the statistical significance of their detection considered over the entire time period of the analysis. For this reason the 4FGL catalog does not contain transient γ -ray sources which are significant over a short duration (such as γ -ray bursts, solar flares, most novae).

The 4FGL catalog builds on several generations of *Fermi*-LAT catalogs (Table 1). It benefits from a number of improvements with respect to 3FGL, besides the twice longer exposure:

1. Pass 8 data¹ were used (§ 2.2). The principal difference relative to the P7REP data used for 3FGL is about 20% larger acceptance at all energies and improved angular resolution above 3 GeV.
2. A new model of underlying diffuse Galactic emission (§ 2.4) was developed.

^{a)} See <https://fermi.gsfc.nasa.gov/ssc/data/access/lat/fl8y/>.

¹ See http://fermi.gsfc.nasa.gov/ssc/data/analysis/documentation/Pass8_usage.html.

| Acronym | Data/IRF/Diffuse model | Energy range/Duration | Sources | Analysis/Reference |
|---------|---------------------------------|-----------------------------|-------------|---|
| 1FGL | P6_V3_DIFFUSE gll_iem_v02 | 0.1 – 100 GeV 11 months | 1451 point | Unbinned, F/B Abdo et al. (2010a) |
| 2FGL | P7SOURCE_V6 gal_2yearp7v6_v0 | 0.1 – 100 GeV 2 years | 1873 point | Binned, F/B Nolan et al. (2012) |
| 3FGL | P7REP_SOURCE_V15 gll_iem_v06 | 0.1 – 300 GeV 4 years | 3033 point | Binned, F/B Acero et al. (2015) |
| FGES | P8R2_SOURCE_V6 gll_iem_v06 | 10 GeV – 2 TeV 6 years | 46 extended | Binned, PSF, $ b < 7^\circ$ Ackermann et al. (2017) |
| 3FHL | P8R2_SOURCE_V6 gll_iem_v06 | 10 GeV – 2 TeV 7 years | 1556 point | Unbinned, PSF Ajello et al. (2017) |
| FHES | P8R2_SOURCE_V6 gll_iem_v06 | 1 GeV – 1 TeV 7.5 years | 24 extended | Binned, PSF, $ b > 5^\circ$ Ackermann et al. (2018) |
| 4FGL | P8R3_SOURCE_V2 new (§ 2.4.1) | 0.05 GeV – 1 TeV 8 years | 5098 point | Binned, PSF this work |

Table 1. The table describes the previous *Fermi*-LAT catalogs mentioned in the text. In the Analysis column, F/B stands for *Front/Back*, PSF for PSF event types^a. In the Sources column, point or extended refer to the catalog’s objective.

^aSee https://fermi.gsfc.nasa.gov/ssc/data/analysis/LAT_essentials.html.

3. We introduced weights in the maximum likelihood analysis (§ 3.2) in order to mitigate the effect of systematic errors due to our imperfect knowledge of the Galactic diffuse emission.
4. We explicitly modeled 75 sources as extended emission regions (§ 3.4), up from 25 in 3FGL.
5. To study the associations of LAT sources with counterparts at other wavelengths, we updated several of the counterpart catalogs, and correspondingly recalibrated the association procedure.

Section 2 describes the LAT, the data and the models for the diffuse backgrounds, celestial and otherwise. Section 3 describes how the catalog is constructed, with emphasis on what has changed since the analysis for the 3FGL catalog. Section 4 describes the catalog itself, while § 5 details the associations and identifications. We provide appendices with technical details of the analysis and of the format of the electronic version of the catalog.

2. INSTRUMENT & BACKGROUND

2.1. *The Large Area Telescope*

The LAT detects γ rays in the energy range 20 MeV to more than 1 TeV, measuring their arrival times, energies, and directions. The field of view of the LAT is 2.4 sr at 1 GeV. The per-photon angular resolution (point-spread function, PSF, 68% containment radius) is $\sim 5^\circ$ at 100 MeV, decreasing to 0.8° at 1 GeV (averaged over the acceptance of the LAT), varying with energy approximately as $E^{-0.8}$ and asymptoting at $\sim 0.1^\circ$ above 20 GeV². The tracking section of the LAT has 36 layers of silicon strip detectors interleaved with 16 layers of tungsten foil (12 thin layers, 0.03 radiation length, at

² See http://www.slac.stanford.edu/exp/glast/groups/canda/lat_Performance.htm.

the top or *Front* of the instrument, followed by 4 thick layers, 0.18 radiation lengths, in the *Back* section). The silicon strips track charged particles, and the tungsten foils facilitate conversion of γ rays to positron-electron pairs. Beneath the tracker is a calorimeter composed of an 8-layer array of CsI crystals (~ 8.5 total radiation lengths) to determine the γ -ray energy. More information about the LAT is provided in [Atwood et al. \(2009\)](#), and the in-flight calibration of the LAT is described in [Abdo et al. \(2009a\)](#), [Ackermann et al. \(2012a\)](#) and [Ackermann et al. \(2012b\)](#).

The LAT is also an efficient detector of the intense background of charged particles from cosmic rays and trapped radiation at the orbit of the *Fermi* satellite. A segmented charged-particle anti-coincidence detector (plastic scintillators read out by photomultiplier tubes) around the tracker is used to reject charged-particle background events. Accounting for γ rays lost in filtering charged particles from the data, the effective collecting area is ~ 8000 cm² at 1 GeV at normal incidence (for the P8R3_SOURCE_V2 event selection used here; see below). The live time is nearly 76%, limited primarily by interruptions of data taking when *Fermi* is passing through the South Atlantic Anomaly ($\sim 15\%$) and readout dead-time fraction ($\sim 9\%$).

2.2. The LAT Data

The data for the 4FGL catalog were taken during the period 2008 August 4 (15:43 UTC) to 2016 August 2 (05:44 UTC) covering eight years. As for 3FGL, intervals around solar flares and bright GRBs were excised. Overall about two days were excised due to solar flares, and 39 ks due to 30 GRBs. The precise time intervals corresponding to selected events are recorded in the GTI extension of the FITS file (Appendix B). The maximum exposure (4.5×10^{11} cm² s at 1 GeV) is reached at the North celestial pole. The minimum exposure (2.7×10^{11} cm² s at 1 GeV) is reached at the celestial equator.

The current version of the LAT data is Pass 8 P8R3 ([Atwood et al. 2013](#); [Bruel et al. 2018](#)). It offers 20% more acceptance than P7REP ([Bregeon et al. 2013](#)) and a narrower PSF at high energies. Both aspects are very useful for source detection and localization ([Ajello et al. 2017](#)). We used the Source class event selection, with the Instrument Response Function (IRF) P8R3_SOURCE_V2. We took advantage of the new PSF event types, which avoid mixing poorly localized events (PSF0) with high-quality ones (PSF3).

The lower bound of the energy range was set to 50 MeV, down from 100 MeV in 3FGL, in order to constrain the spectra better at low energy. It does not help detecting or localizing sources because of the very broad PSF below 100 MeV. The upper bound was raised from 300 GeV in 3FGL to 1 TeV. This is because as the source-to-background ratio decreases, the sensitivity curve (Figure 18 of [Abdo et al. 2010a](#), 1FGL) shifts to higher energies. The 3FHL catalog ([Ajello et al. 2017](#)) went up to 2 TeV, but only 566 events exceed 1 TeV over 8 years (to be compared to 714 thousands above 10 GeV).

2.3. Zenith angle selection

The zenith angle cut was set such that the contribution of the Earth limb at that zenith angle was less than 10% of the total background. Integrated over all zenith angles, the residual Earth limb contamination is less than 1%. We kept PSF3 event types with zenith angles less than 80° between 50 and 100 MeV, PSF2 and PSF3 event types with zenith angles less than 90° between 100 and 300 MeV, and PSF1, PSF2 and PSF3 event types with zenith angles less than 100° between 300 MeV and 1 GeV. Above 1 GeV we kept all events with zenith angles less than 105° (Table 2).

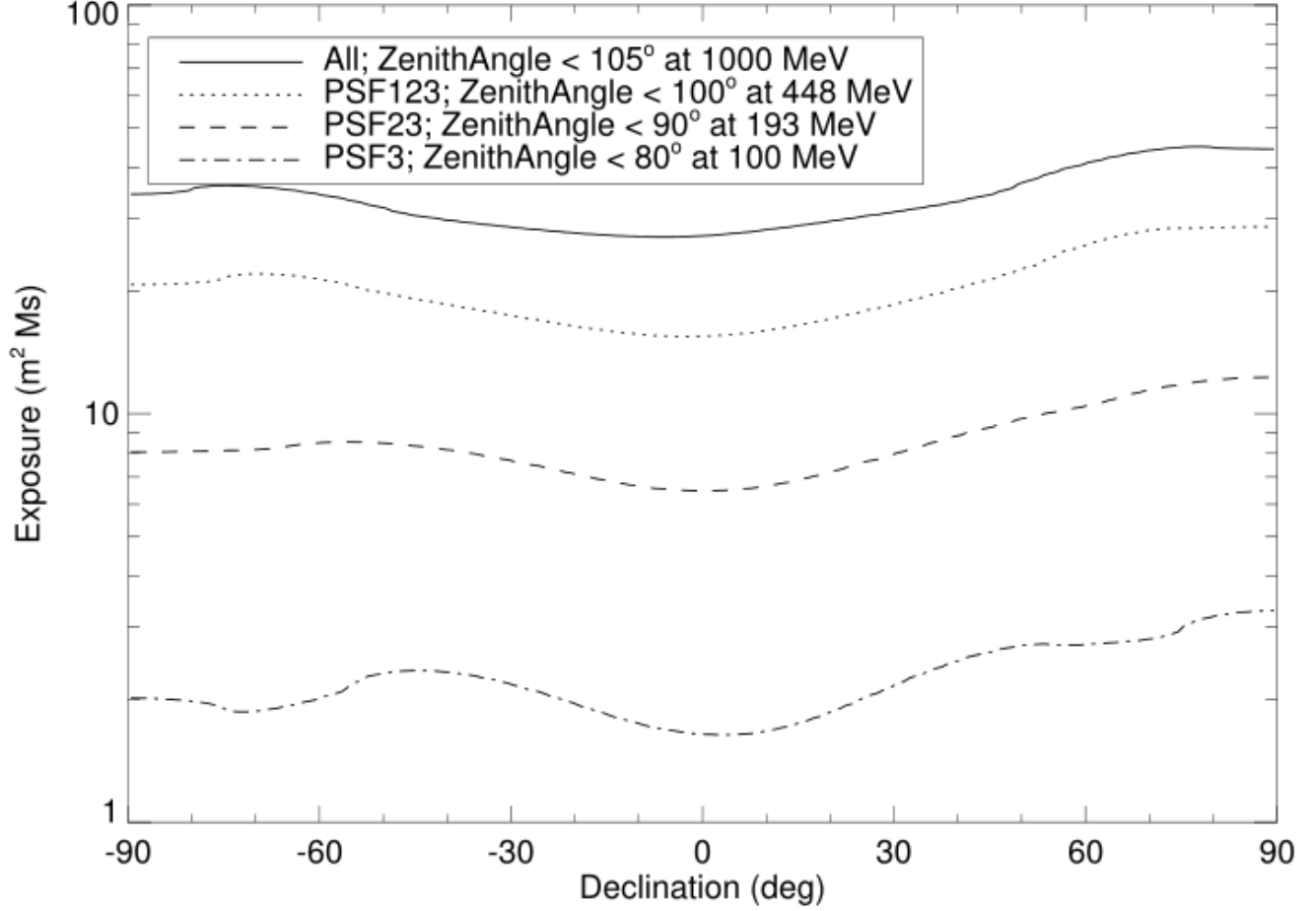


Figure 1. Exposure as a function of declination and energy, averaged over right ascension, summed over all relevant event types as indicated in the figure legend.

| Energy interval (GeV) | NBins | ZMax (deg) | Ring width (deg) | Pixel size (deg) | | | | |
|--------------------------|-------|---------------|---------------------|------------------|------|------|------|------|
| | | | | PSF0 | PSF1 | PSF2 | PSF3 | All |
| 0.05 – 0.1 | 3 | 80 | 7 | ... | ... | ... | 0.6 | |
| 0.1 – 0.3 | 5 | 90 | 7 | ... | ... | 0.6 | 0.6 | |
| 0.3 – 1 | 6 | 100 | 5 | ... | 0.4 | 0.3 | 0.2 | |
| 1 – 3 | 5 | 105 | 4 | 0.4 | 0.15 | 0.1 | 0.1 | |
| 3 – 10 | 6 | 105 | 3 | 0.25 | 0.1 | 0.05 | 0.04 | |
| 10 – 1000 | 10 | 105 | 2 | ... | ... | ... | ... | 0.04 |

Table 2. The 15 components (all in binned mode) of the Summed Likelihood approach used in 4FGL. Components in a given energy interval share the same number of energy bins, the same zenith angle selection and the same RoI size, but have different pixel sizes in order to adapt to the PSF width. Each filled entry under Pixel size corresponds to one component of the summed likelihood. NBins is the number of energy bins in the interval, ZMax is the zenith angle cut, Ring width refers to the difference between the RoI core and the extraction region, as explained in item 5 of § 3.2.

The resulting integrated exposure over 8 years is shown on Figure 1. The dependence on declination is due to the combination of the inclination of the orbit, the rocking angle and the off-axis effective area. The north-south asymmetry is due to the south-Atlantic anomaly over which the instrument is switched off. Because of the regular precession of the orbit every 53 days, the dependence on right ascension is small when averaged over long periods of time. The dependence on energy is due to the increase of the effective area up to 1 GeV, and the addition of new event types at 100 MeV, 300 MeV and 1 GeV. The off-axis effective area depends somewhat on energy and event type. This introduces a slight dependence of the shape of the curve on energy.

Selecting on zenith angle applies a kind of time selection (which depends on direction in the sky). This means that the effective time selection at low energy is not exactly the same as at high energy. The periods of time during which a source is at zenith angle $< 105^\circ$ but (for example) $> 90^\circ$ last typically a few minutes every orbit. This is shorter than the main variability time scales of astrophysical sources, and therefore not a concern. There remains however the modulation due to the precession of the spacecraft orbit on longer time scales over which blazars can vary. This is not a problem for a catalog (it can at most appear as a spectral effect, and should average out when considering statistical properties) but it should be kept in mind when extracting spectral parameters of individual variable sources. We used the same zenith angle cut for all event types in a given energy interval in order to reduce systematics due to that time selection.

Because the data are limited by systematics at low energies everywhere in the sky (Appendix A) rejecting half of the events below 300 MeV and 75% of them below 100 MeV does not impact the sensitivity (if we had kept these events, the weights would have been lower).

2.4. Model for the Diffuse Gamma-Ray Background

2.4.1. Diffuse emission of the Milky Way

We extensively updated the model for Galactic diffuse emission for the 4FGL analysis, using the same P8R3 data selections (PSF types, energy ranges, and zenith angle limits). The development of the model will be described in detail elsewhere. Here we summarize the primary differences from the model developed for the 3FGL catalog (Acero et al. 2016a). In both cases, the model is based on linear combinations of templates representing components of the Galactic diffuse emission. For 4FGL we updated all of the templates, and added a new one as described below.

We have adopted the new, all-sky high-resolution, 21-cm spectral line HI4PI survey (HI4PI Collaboration et al. 2016) as our tracer of H I, and extensively refined the procedure for partitioning the H I and H₂ (traced by the 2.6-mm CO line) into separate ranges of Galactocentric distance (‘rings’), by decomposing the spectra into individual line profiles, so the broad velocity dispersion of a massive interstellar clouds does not effectively distribute its emission very broadly along the line of sight. We also updated the rotation curve, and adopted a new procedure for interpolating the rings across the Galactic center and anticenter, now incorporating a general model for the surface density distribution of the interstellar medium to inform the interpolation, and defining separate rings for the Central Molecular Zone (within ~ 150 pc of the Galactic center and between 150 pc and 600 pc of the center). With this approach, the Galaxy is divided into ten concentric rings.

The template for the inverse Compton emission is still based on a model interstellar radiation field and cosmic-ray electron distribution (calculated in GALPROP v56, described in Porter et al. 2017)³ but now we formally subdivide the model into rings (with the same Galactocentric radius ranges as for the gas templates), which are fit separately in the analysis, to allow some spatial freedom relative to the static all-sky inverse-Compton model.

We have also updated the template of the ‘dark gas’ component, representing interstellar gas that is not traced by the HI and CO line surveys, by comparison with the Planck dust optical depth map⁴. The dark gas is inferred as the residual component after the best-fitting linear combination of total $N(\text{HI})$ and W_{CO} are subtracted, i.e., as the component not correlated with the atomic and molecular gas spectral line tracers, in a procedure similar to that used in Acero et al. (2016a). In particular, as before we retained the negative residuals as a ‘column density correction map’.

New with the 4FGL model we incorporated a template representing the contribution of unresolved Galactic sources, derived based on a model spatial distribution and luminosity function developed based on the distribution of Galactic sources in Acero et al. (2015) and an analytical evaluation of the flux limit for source detection as a function of direction on the sky.

As for the 3FGL-era model, we iteratively determined and re-fit a model component that represents non-template diffuse γ -ray emission, primarily Loop I and the *Fermi* bubbles. To avoid overfitting the residuals, and possibly suppressing faint Galactic sources, we spectrally and spatially smoothed the residual template.

The model fitting was performed using Gardian, as a summed likelihood analysis. This procedure involves transforming the ring maps described above into spatial-spectral templates evaluated in GALPROP. We used a model from Ackermann et al. (2012c), $^S\text{L}^Z6^R30^T150^C2$. The model is a linear combination of these templates, with free scaling functions of various forms for the individual templates. For components with the largest contributions, a piecewise continuous function, linear in the logarithm of energy, with nine degrees of freedom was used. Other components had a similar scaling function with five degrees of freedom, or power-law scaling, or overall scale factors, chosen to give the model adequate freedom while reducing the overall number of free parameters. The model also required a template for the point and small-extended sources in the sky. We iterated the fitting using preliminary versions of the 4FGL catalog. This template was also given spectral degrees of freedom. Other diffuse templates, described below and not related to Galactic emission, were included in the model fitting.

2.4.2. Isotropic background

The isotropic diffuse background was derived from all-sky fits of the eight-year data set using the Galactic diffuse emission model described above and a preliminary version of the 4FGL catalog. The diffuse background includes charged particles misclassified as γ rays. We implicitly assume that the acceptance for these residual charged particles is the same as for γ rays in treating these diffuse background components together. For the analysis we derived the contributions to the isotropic background separately for all event types.

2.4.3. Solar and lunar template

³ <http://galprop.stanford.edu>

⁴ COM.CompMapDust-GNILC-Model-Opacity_2048_R2.01.fits, Planck Collaboration et al. (2016)

The quiescent Sun and the Moon are fairly bright γ -ray sources. The Sun moves in the ecliptic but the solar γ -ray emission is extended because of cosmic-ray interactions with the solar radiation field; detectable emission from inverse Compton scattering of cosmic-ray electrons on the radiation field of the Sun extends several degrees from the Sun (Abdo et al. 2011). The Moon is not an extended source in this way but the lunar orbit is inclined somewhat relative to the ecliptic and the Moon moves through a larger fraction of the sky than the Sun. Averaged over time, the γ -ray emission from the Sun and Moon trace a region around the ecliptic. Without any correction this can seriously affect the spectra and light curves, so starting with 3FGL we model that emission.

The Sun and Moon emission are modulated by the solar magnetic field which deflects cosmic rays more (and therefore reduces γ -ray emission) when the Sun is at maximum activity. For that reason the model used in 3FGL (based on the first 18 months of data when the Sun was near minimum) was not adequate for 8 years. We used the improved model of the Moon (Ackermann et al. 2016a) and a data-based model of the solar disk and inverse Compton scattering on the solar light (S. Raino, private communication).

We combined those models with calculations of their motions and of the exposure of the observations by the LAT to make templates for the equivalent diffuse component over 8 years using *gtsuntemp* (Johannesson et al. 2013). For 4FGL we used two different templates: one for the inverse Compton emission on the solar light (pixel size $0^\circ:25$) and one for the sum of the solar and lunar disks. For the latter we reduced the pixel size to $0^\circ:125$ in order to describe the disks accurately, and computed a specific template for each event type / maximum zenith angle combination of Table 2 (because their exposure maps are not identical). As for 3FGL those components have no free parameter.

2.4.4. Residual Earth limb template

For 3FGL we reduced the low-energy Earth limb emission by selecting zenith angles less than 100° , and modeled the residual contamination approximately. For 4FGL we chose to cut harder on zenith angle at low energies and select event types with the best PSF (§ 2.3). That procedure eliminates the need for a specific Earth limb component in the model.

3. CONSTRUCTION OF THE CATALOG

The procedure used to construct the 4FGL catalog has a number of improvements relative to that of the 3FGL catalog. In this section we review the procedure, emphasizing what was done differently. The significances (§ 3.2) and spectral parameters (§ 3.3) of all catalog sources were obtained using the standard *pyLikelihood* framework (Python analog of *gtlike*) in the LAT Science Tools⁵ (version v11r7p0). The localization procedure (§ 3.1), which relies on *pointlike*, provided the source positions, the starting point for the spectral fitting, and a comparison for estimating the reliability of the results (§ 3.5.2).

Throughout the text we denote as RoIs, for Regions of Interest, the regions in which we extract the data. We use the Test Statistic $TS = 2(\log \mathcal{L} - \log \mathcal{L}_0)$ (Mattox et al. 1996) to quantify how significantly a source emerges from the background, comparing the maximum value of the likelihood function \mathcal{L} over the RoI including the source in the model with \mathcal{L}_0 , the value without the source.

3.1. Detection and Localization

⁵ See <http://fermi.gsfc.nasa.gov/ssc/data/analysis/documentation/Cicerone/>.

This section describes the generation of a list of candidate sources, with locations and initial spectral fits. This initial stage uses *pointlike* (Kerr 2010). Compared with the *gtlike*-based analysis described in § 3.2 to 3.5, it uses the same time range and IRFs, but the partitioning of the sky, the weights, the computation of the likelihood function and its optimization are independent. Energy dispersion is neglected. Events below 100 MeV are useless for source detection and localization, and are ignored at this stage. Since this version of the computation of the likelihood function is used for localization, it needs to represent a valid estimate of the probability of observing a point source with the assumed spectral function.

The process started with an initial set of sources from the 3FGL analysis, not just those reported in that catalog, but also including all candidates failing the significance threshold (i.e., with $10 < TS < 25$). It used the 75 spatially extended sources listed in § 3.4, and the three-source representation of the Crab (§ 3.3). The same spectral models were considered for each source as in § 3.3, but the favored model (power law or curved) was not necessarily the same.

The generation of a candidate list of sources, with locations and initial spectral fits is substantially the same as for 3FGL. The sky was partitioned using HEALPix⁶ (Górski et al. 2005) with $N_{\text{side}} = 12$, resulting in 1728 tiles of ~ 25 deg² area. The RoIs included events in cones of 5° radius about the center of the tiles. The data were binned into 16 energy bands from 100 MeV to 1 TeV (up from 14 bands to 316 GeV in 3FGL), and, as before, separated into the *Front* and *Back* event types. However, only *Front* events were used below 316 MeV, to avoid the poor PSF and contribution of the Earth limb. All sources within the tile and those nearby, in the adjacent and second rings, were included in the model. Only the spectral models and positions of sources within the central tile were allowed to vary to optimize the likelihood. To account for correlations with fixed nearby sources, and a factor of three overlap for the data, iterations were performed until log likelihoods for all RoIs changed by less than 10.

We assumed here that the isotropic spectrum was exactly constant over the sky, but readjusted the Galactic diffuse emission. Starting with a version of the Galactic diffuse model (§ 2.4.1) without its non-template diffuse γ -ray emission, we derived an alternative adjustment by optimizing the Galactic diffuse normalization for each RoI and the eight bands below 10 GeV. These numbers were turned into an 8-layer map which was smoothed, then applied to the diffuse model itself. Then the corrections were measured again. This process converged after two iterations, such that no more corrections were needed. The advantage of the procedure, compared to fitting parameters in each RoI (§ 3.2), is that the effective predictions do not vary abruptly from an RoI to its neighbors.

After a set of iterations had converged, the localization procedure was applied, and source positions updated for a new set of iterations. At this stage, new sources were occasionally added using the residual *TS* procedure described below. The detection and localization process resulted in ~ 8020 candidate point sources with $TS > 10$. The fit validation and likelihood weighting were done as in 3FGL.

3.1.1. Detection of additional sources

As for 3FGL, the same implementation of the likelihood used for optimizing source parameters was used to test for the presence of additional point sources. This is inherently iterative, in that the likelihood is valid to the extent that it represents an accurate measure of the model prediction. Thus

⁶ <http://healpix.sourceforge.net>.

| α | β | E_0 (GeV) | Comment |
|----------|---------|-------------|--------------------------|
| 1.7 | 0.0 | 50.00 | Hard |
| 2.2 | 0.0 | 1.00 | Intermediate |
| 2.7 | 0.0 | 0.25 | Soft |
| 2.0 | 0.5 | 2.00 | Curved, but not a pulsar |
| 2.0 | 0.3 | 1.00 | Pulsar-like |

Table 3. The table describes the five spectral shapes used for source finding in 4FGL. The spectral parameters α , β and E_0 refer to the LogParabola spectral shape (Eq. 2).

source detection depends on having nearby stronger sources already included. Since 3FGL was based on four years of data, one can expect many more sources. As we accumulated more and more data since then, the source list gradually evolved. A measure of success is that subsequent source finding adds little to the total. As before, an iteration starts with choosing a HEALPix $N_{side} = 128$ grid, 3.1 M points with average separation 0.15 degrees. But now, instead of testing a single power-law spectrum, we try five spectral shapes; three are power laws with different indices, two with significant curvature. Table 3 lists the spectral shapes used for the templates.

For each trial position, and each of the five templates, the normalizations were optimized, and the resulting TS associated with the pixel. Then, as before, but independently for each template, a cluster analysis selected groups of pixels with $TS > 16$, as compared to $TS > 10$ for 3FGL. Each cluster defined a seed, with a position defined by weighting the TS values. Finally, the five sets of potential seeds were compared, and, for those within 1° , the seed with the largest TS was selected for inclusion.

3.1.2. Localization

The position of each source was determined by maximizing the likelihood with respect to its position only. That is, all other parameters are kept fixed. The possibility that a shifted position would affect the spectral models or positions of nearby sources is accounted for by iteration. Ideally the log likelihood is a quadratic form in any pair of angular variables, assuming small angular offsets. We define LTS, for Localization Test Statistic, to be twice the log of the likelihood ratio of any position with respect to the maximum; the LTS evaluated for a grid of positions is called an LTS map. We fit the distribution of LTS to a quadratic form to determine the uncertainty ellipse, the major and minor axes and orientation. We also define a measure, the localization quality (LQ), of how well the actual LTS distribution matches this expectation by reporting the sum of the squares of the deviations of eight points evaluated from the fit at a circle of radius corresponding to twice the geometric mean of the two Gaussian sigmas.

We flagged apparently significant sources that do not have good localization fits ($LQ > 8$) with Flag 9 (Table 5) and for them estimated the position and uncertainty by performing a moment analysis of the LTS function instead of fitting a quadratic form. Some sources that did not have a well-defined peak in the likelihood were discarded by hand, on the consideration that they were most likely related to residual diffuse emission. Another possibility is that two adjacent sources produce a dumbbell-like shape; for a few of these cases we added a new source by hand.

As in 3FGL, we checked the brightest sources spatially associated with likely multiwavelength counterparts, comparing their localizations with the well-measured positions of the counterparts. The

smaller statistical source localization errors in 4FGL allowed us to estimate the absolute precision Δ_{abs} (at the 95% confidence level) more accurately to $\sim 0^{\circ}.0075$, up from $\sim 0^{\circ}.005$ in 3FGL. The systematic factor f_{rel} was the same 1.05 as in 3FGL. Eq. 1 shows how the statistical errors Δ_{stat} are transformed into total errors Δ_{tot} :

$$\Delta_{\text{tot}}^2 = (f_{\text{rel}} \Delta_{\text{stat}})^2 + \Delta_{\text{abs}}^2 \quad (1)$$

applies to the two ellipse axes separately.

3.2. Significance and Thresholding

The framework for this stage of the analysis is inherited from the 3FGL catalog. It splits the sky into RoIs, varying typically half a dozen sources near the center of the RoI at the same time. There are 1748 RoIs for 4FGL, listed in the `ROI`s extension of the catalog (Appendix B). The global best fit is reached iteratively, injecting the spectra of sources in the outer parts of the RoI from the previous step or iteration. In this approach the diffuse emission model (§ 2.4) is taken from the global templates (including the spectrum, unlike what is done with *pointlike* in § 3.1) but it is modulated in each RoI by three parameters: normalization (at 1 GeV) and small corrective slope of the Galactic component and normalization of the isotropic component.

Among more than 8,000 seeds coming from the localization stage, we keep only sources with $TS > 25$, corresponding to a significance of just over 4σ evaluated from the χ^2 distribution with 4 degrees of freedom (position and spectral parameters of a power-law source, [Mattox et al. 1996](#)). The model for the current RoI is readjusted after removing each seed below threshold, so that the final model fits the full data. The low-energy flux of the seeds below threshold (a fraction of which are real sources) can be absorbed by neighboring sources closer than the PSF radius.

As in 3FGL we manually added known LAT pulsars that could not be localized by the automatic procedure without phase selection. However none of those reached $TS > 25$ in 4FGL.

We introduced a number of improvements with respect to 3FGL (by decreasing order of importance):

1. In 3FGL we had already noted that systematic errors due to an imperfect modeling of diffuse emission were larger than statistical errors in the Galactic plane, and at the same level over the entire sky. With twice as much exposure and an improved effective area at low energy with Pass 8, the effect now dominates. The approach adopted in 3FGL (comparing runs with different diffuse models) allowed characterizing the effect globally and flagging the worst offenders, but left purely statistical errors on source parameters. In 4FGL we introduce weights in the maximum likelihood approach (Appendix A). This allows obtaining directly (although in an approximate way) smaller TS and larger parameter errors, reflecting the level of systematic uncertainties. We estimated the relative spatial and spectral residuals in the Galactic plane where the diffuse emission is strongest. The resulting systematic level $\epsilon \sim 3\%$ was used to compute the weights. This is by far the most important improvement, which avoids reporting many dubious soft sources.
2. The automatic iteration procedure at the next-to-last step of the process was improved. There are now two iteration levels. In a standard iteration the sources and source models are fixed and only the parameters are free. An RoI and all its neighbors are run again until $\log \mathcal{L}$ does not change by more than 10 from the previous iteration. Around that we introduce another

iteration level (superiterations). At the first iteration of a given superiteration we reenter all seeds and remove (one by one) those with $TS < 16$. We also systematically check curvature significance (§ 3.3) at this first iteration, and allow sources to switch to a curved spectral shape if $TS_{\text{curv}} > 9$ or force them back to power law if $TS_{\text{curv}} < 9$ (§ 3.3). At the end of a superiteration an RoI (and its neighbors) enters the next superiteration until $\log \mathcal{L}$ does not change by more than 10 from the last iteration of the previous superiteration. This procedure stabilizes the spectral shapes, particularly in the Galactic plane. Seven superiterations were required to reach full convergence.

3. The fits are now performed from 50 MeV to 1 TeV, and the overall significances (**Signif_Avg**) as well as the spectral parameters refer to the full band. The total energy flux, on the other hand, is still reported between 100 MeV and 100 GeV. For hard sources with photon index less than 2 integrating up to 1 TeV would result in much larger uncertainties. The same is true for soft sources with photon index larger than 2.5 when integrating down to 50 MeV.
4. We considered the effect of energy dispersion, in the approximate way implemented in the Science Tools. The effect of energy dispersion is calculated globally for each source, and applied to the whole 3D model of that source, rather than accounting for energy dispersion separately in each pixel. This approximate rescaling captures the main effect at a very minor computational cost. The effect of energy dispersion on the spectra is relatively small. It tends to increase the energy flux (by 4% on average), to reduce the width of the power-law index distribution (by making hard sources softer and soft sources harder, but changing the index by less than 0.02), and to make spectra more curved (because energy dispersion acts as a convolution) but increasing β by only 0.01 on average. In evaluating the likelihood function the effects of energy dispersion were not applied to the isotropic background and the Sun/Moon components whose spectra were obtained from the data without considering energy dispersion.
5. We used smaller RoIs at higher energy because we are interested in the core region only, which contains the sources whose parameters come from that RoI (sources in the outer parts of the RoI are entered only as background). The core region is the same for all energy intervals, and the RoI is obtained by adding a ring to that core region, whose width adapts to the PSF and therefore decreases with energy (Table 2). This does not affect the result because the outer parts of the RoI would not have been correlated to the inner sources at high energy anyway, but saves memory and CPU time.
6. At the last step of the fitting procedure we tested all spectral shapes described in § 3.3 (including log-normal for pulsars and cutoff power law for other sources), readjusting the parameters (but not the spectral shapes) of neighboring sources.

We used only binned likelihood analysis in 4FGL because unbinned mode is much more CPU intensive, and does not support weights or energy dispersion. We split the data into fifteen components, selected according to PSF event type and described in Table 2. As explained in § 2.4.4 at low energy we kept only the event types with the best PSF. Each event type selection has its own isotropic diffuse template (because it includes residual charged-particle background, which depends on event type). A single component is used above 10 GeV in order to save memory and CPU time: at high

energy the background under the PSF is small, so keeping the event types separate does not improve significance very much; it would help for localization, but this is done separately (§ 3.1.2).

A known inconsistency in acceptance exists between Pass 8 PSF event types. It is easy to see on bright sources or the entire RoI spectrum and peaks at the level of 10% between PSF0 (positive residuals, underestimated effective area) and PSF3 (negative residuals, overestimated effective area) at a few GeV. In that range all event types were considered so the effect on source spectra should be minor. Below 1 GeV the PSF0 event type was discarded so the inconsistency could introduce a downward bias (appearing as slightly too hard spectra) but the discrepancy is lower at low energy. The bias on power-law index is estimated to be ~ -0.01 .

3.3. Spectral Shapes

The spectral representation of sources largely follows what was done in 3FGL, considering three spectral models (power law, power law with subexponential cutoff, log-normal). We changed two important things in the way we parametrize the cutoff power law:

- The cutoff energy was replaced by an exponential factor (a in Eq. 3) which is allowed to be positive. This makes the simple power law a special case of the cutoff power law and allows fitting that model to all sources.
- We set the exponential index (b in Eq. 3) to 2/3 (instead of 1) for all pulsars that are too faint for it to be left free. This recognizes the fact that $b < 1$ (subexponential) in all bright pulsars. Among the six brightest pulsars, three have $b \sim 0.55$ and three have $b \sim 0.75$). We chose 2/3 as a simple intermediate value.

Therefore the spectral representations which can be found in 4FGL are:

- a log-normal representation (`LogParabola` in the tables) for all significantly curved spectra except pulsars, 3C 454.3 and the Small Magellanic Cloud (SMC):

$$\frac{dN}{dE} = K \left(\frac{E}{E_0} \right)^{-\alpha - \beta \log(E/E_0)} \quad (2)$$

where \log is the natural logarithm. The reference energy E_0 is set to `Pivot_Energy` in the tables. The parameters K , α (spectral slope at E_0) and the curvature β appear as `LP_Flux_Density`, `LP_Index` and `LP_beta` in the tables, respectively. No significantly negative β (spectrum curved upwards) was found. The maximum allowed β was set to 1 as in 3FGL.

- a subexponentially cutoff power law for all significantly curved pulsars (`PLSuperExpCutoff` in the tables):

$$\frac{dN}{dE} = K \left(\frac{E}{E_0} \right)^{-\Gamma} \exp(a(E_0^b - E^b)) \quad (3)$$

where E_0 and E in the exponential are expressed in MeV. The reference energy E_0 is set to `Pivot_Energy` in the tables and the parameters K , Γ (low-energy spectral slope), a (exponential factor in MeV^{-b}) and b (exponential index) appear as `PLEC_Flux_Density`, `PLEC_Index`, `PLEC_Expfactor` and `PLEC_Exp_Index` in the tables, respectively. Note that in the Science Tools that spectral shape is called `PLSuperExpCutoff2` and no E_0^b term appears in the exponential,

so the error on K in the tables was obtained from the covariance matrix. The minimum Γ was set to 0 (in 3FGL it was set to 0.5, but a smaller b results in a smaller Γ). No significantly negative a (spectrum curved upwards) was found.

- a simple power-law form (Eq. 3 without the exponential term) for all sources not significantly curved. For those parameters K and Γ appear as `PL_Flux_Density` and `PL_Index` in the tables.

A source is considered significantly curved if $TS_{\text{curv}} > 9$ (3σ significance) where $TS_{\text{curv}} = 2 \log(\mathcal{L}(\text{curved spectrum})/\mathcal{L}(\text{power-law}))$. When this is achieved the global model (used to fit neighboring sources) uses the curved representation. We used a lower TS_{curv} threshold than in 3FGL (where it was 16, or 4σ) for two reasons. First, all bright sources are actually significantly curved downwards so there is no good reason to penalize the curved models too much. Second, the power-law model tends to exceed the data at both ends of the spectrum, where constraints are weak. It is not a worry at high energy, but at low energy the collection of faint sources modeled as power laws generates an effectively diffuse excess in the model, which will make the curved sources more curved than they should be. Using a `LogParabola` spectral shape for all sources would be even better physically, but the very large correlation between sources at low energy due to the broad PSF makes that unstable. The curvature significance ($\sqrt{TS_{\text{curv}}}$) is reported as `LP_SigCurv` or `PLEC_SigCurv`.

Sources with curved spectra are considered significant whenever $TS > 25 + 9 = 34$. This is conservative enough, and accepts a few more strongly curved faint sources (pulsar-like) than the 3FGL criterion which requested $TS > 25$ in the power-law representation.

One more pulsar (PSR J1057–5226) was fit with a free exponential index, besides the six sources modeled in this way in 3FGL. The Crab was modeled with three spectral components as in 3FGL, but the inverse Compton emission of the nebula was represented as a log-normal law instead of a simple power law. The parameters of that component were fixed to $\alpha = 1.75$, $\beta = 0.08$, $K = 5.5 \times 10^{-13}$ ph/cm²/MeV/s at 10 GeV, mimicking the broken power-law fit by [Buehler et al. \(2012\)](#). They were unstable (too much correlation with the pulsar) without phase selection. Four other sources had fixed parameters in 3FGL. These were freed in 4FGL.

Overall in 4FGL seven sources (the six brightest pulsars and 3C 454.3) were fit as `PLSuperExpCutoff` with free b (Eq. 3), 215 pulsars were fit as `PLSuperExpCutoff` with $b = 2/3$, the SMC was fit as `PLSuperExpCutoff` with $b = 1$, 1332 sources were fit as `LogParabola` (including the fixed inverse Compton component of the Crab and 38 other extended sources) and the rest were represented as power laws. The larger fraction of curved spectra compared to 3FGL is due to the lower TS_{curv} threshold.

The way the parameters are reported has changed as well:

- The spectral shape parameters are now explicitly associated to the spectral model they come from. They are reported as `Shape_Param` where `Shape` is one of `PL` (`PowerLaw`), `PLEC` (`PLSuperExpCutoff`) or `LP` (`LogParabola`) and `Param` is the parameter name. Columns `Shape_Index` replace `Spectral_Index` which was ambiguous.
- All sources were fit with the three spectral shapes, so all fields are filled. The curvature significance is calculated twice by comparing power law with both log-normal and exponentially cutoff power law (although only one is actually used to switch to the curved shape in the global model, depending on whether the source is a pulsar or not). There are also three `Shape_Flux_Density` columns referring to the same `Pivot_Energy`.

This representation allows comparing unassociated sources with either pulsars or blazars using the same spectral shape. The preferred spectral shape (reported as `SpectrumType`) remains what is used in the global model, when the source is part of the background (i.e., when fitting the other sources). It is also what is used to derive the fluxes, their uncertainties and the significance.

3.4. *Extended Sources*

As for the 3FGL catalog, we explicitly model as spatially extended those LAT sources that have been shown in dedicated analyses to be resolved by the LAT. The catalog process does not involve looking for new extended sources, testing possible extension of sources detected as point-like, nor refitting the spatial shapes of known extended sources.

Most templates are geometrical, so they are not perfect matches to the data and the source detection often finds residuals on top of extended sources, which are then converted into additional point sources. As in 3FGL those additional point sources were voluntarily deleted from the model, except if they met two of the following criteria: associated, much harder than the extended source (`Pivot_Energy` larger by a factor e or more), very significant ($TS > 100$). Contrary to 3FGL, that procedure was applied inside the Cygnus X cocoon as well.

The latest pre-4FGL compilation is the 55 extended sources entered in 3FHL, which includes the result of the systematic search for new sources in the Galactic plane ($|b| < 7^\circ$) above 10 GeV (FGES, [Ackermann et al. 2017](#)). Two of those were not propagated to 4FGL:

- FGES J1800.5–2343 was replaced by the W 28 template from 3FGL, and the nearby excesses ([Hanabata et al. 2014](#)) were left to be modeled as point sources.
- FGES J0537.6+2751 was replaced by the radio template of S 147 used in 3FGL, which fits better than the disk used in the FGES paper (S 147 is a soft source, so it was barely detected above 10 GeV).

MSH 15-56 was replaced by two morphologically distinct components, following [Devin et al. \(2018\)](#): one for the SNR (SNR mask in the paper), the other one for the PWN inside it (radio template). We added back the W 30 SNR on top of FGES J1804.7–2144 (coincident with HESS J1804–216). The two overlap but the best localization clearly moves with energy from W 30 to HESS J1804–216.

Eighteen sources were added, resulting in 75 extended sources in 4FGL:

- The Rosette nebula and Monoceros SNR (too soft to be detected above 10 GeV) were characterized by [Katagiri et al. \(2016b\)](#). We used the same templates.
- The systematic search for extended sources outside the Galactic plane above 1 GeV (FHES, [Ackermann et al. 2018](#)) found sixteen reliable extended sources. Five of them were already known as extended sources. We ignored two others: M 31 (extension only marginally significant) and SNR G119.5+10.2 around PSR J0007+7303 (not significant without phase gating). We introduced the nine remaining FHES sources (including the Crab nebula and the ρ Oph molecular cloud). One of them (J1741.6-3917) was reported by [Araya \(2018a\)](#) as well, with similar extension.
- Four HESS sources were found to be extended sources in the *Fermi* range as well: J1534-571 ([Araya 2017](#)), J1808-204 ([Yeung et al. 2016](#)), J1809-193 and J1813-178 ([Araya 2018b](#)).

- Three extended sources were discovered in the search for GeV emission from magnetars (Li et al. 2017a). They contain SNRs (Kes 73, Kes 79 and G42.8+0.6 respectively) but are much bigger than the radio SNRs. One of them (around Kes 73) was also noted by Yeung et al. (2017).

Table 4 lists the source name, origin, spatial template and the reference for the dedicated analysis. These sources are tabulated with the point sources, with the only distinction being that no position uncertainties are reported and their names end in e (see Appendix B). Unidentified point sources inside extended ones are indicated as “xxx field” in the ASSOC2 column of the catalog.

Table 4. Extended Sources Modeled in the 4FGL Analysis

| 4FGL Name | Extended Source | Origin | Spatial Form | Extent [deg] | Reference |
|---------------|---------------------|---------|------------------|--------------|--------------------------|
| J0058.0–7245e | SMC Galaxy | Updated | Map | 1.5 | Caputo et al. (2016) |
| J0221.4+6241e | HB 3 | New | Disk | 0.8 | Katagiri et al. (2016a) |
| J0222.4+6156e | W 3 | New | Map | 0.6 | Katagiri et al. (2016a) |
| J0322.6–3712e | Fornax A | 3FHL | Map | 0.35 | Ackermann et al. (2016c) |
| J0427.2+5533e | SNR G150.3+4.5 | 3FHL | Disk | 1.515 | Ackermann et al. (2017) |
| J0500.3+4639e | HB 9 | New | Map | 1.0 | Araya (2014) |
| J0500.9–6945e | LMC FarWest | 3FHL | Map ^a | 0.9 | Ackermann et al. (2016d) |
| J0519.9–6845e | LMC Galaxy | New | Map ^a | 3.0 | Ackermann et al. (2016d) |
| J0530.0–6900e | LMC 30DorWest | 3FHL | Map ^a | 0.9 | Ackermann et al. (2016d) |
| J0531.8–6639e | LMC North | 3FHL | Map ^a | 0.6 | Ackermann et al. (2016d) |
| J0534.5+2201e | Crab nebula IC | New | Gaussian | 0.03 | Ackermann et al. (2018) |
| J0540.3+2756e | S 147 | 3FGL | Disk | 1.5 | Katsuta et al. (2012) |
| J0617.2+2234e | IC 443 | 2FGL | Gaussian | 0.27 | Abdo et al. (2010b) |
| J0634.2+0436e | Rosette | New | Map | (1.5, 0.875) | Katagiri et al. (2016b) |
| J0639.4+0655e | Monoceros | New | Gaussian | 3.47 | Katagiri et al. (2016b) |
| J0822.1–4253e | Puppis A | 3FHL | Disk | 0.443 | Ackermann et al. (2017) |
| J0833.1–4511e | Vela X | 2FGL | Disk | 0.91 | Abdo et al. (2010c) |
| J0851.9–4620e | Vela Junior | 3FHL | Disk | 0.978 | Ackermann et al. (2017) |
| J1023.3–5747e | Westerlund 2 | 3FHL | Disk | 0.278 | Ackermann et al. (2017) |
| J1036.3–5833e | FGES J1036.3–5833 | 3FHL | Disk | 2.465 | Ackermann et al. (2017) |
| J1109.4–6115e | FGES J1109.4–6115 | 3FHL | Disk | 1.267 | Ackermann et al. (2017) |
| J1208.5–5243e | SNR G296.5+10.0 | 3FHL | Disk | 0.76 | Acero et al. (2016b) |
| J1213.3–6240e | FGES J1213.3–6240 | 3FHL | Disk | 0.332 | Ackermann et al. (2017) |
| J1303.0–6312e | HESS J1303–631 | 3FGL | Gaussian | 0.24 | Aharonian et al. (2005) |
| J1324.0–4330e | Centaurus A (lobes) | 2FGL | Map | (2.5, 1.0) | Abdo et al. (2010d) |
| J1355.1–6420e | HESS J1356–645 | 3FHL | Disk | 0.405 | Ackermann et al. (2017) |
| J1409.1–6121e | FGES J1409.1–6121 | 3FHL | Disk | 0.733 | Ackermann et al. (2017) |
| J1420.3–6046e | HESS J1420–607 | 3FHL | Disk | 0.123 | Ackermann et al. (2017) |
| J1443.0–6227e | RCW 86 | 3FHL | Map | 0.3 | Ajello et al. (2016) |
| J1501.0–6310e | FHES J1501.0–6310 | New | Gaussian | 1.29 | Ackermann et al. (2018) |
| J1507.9–6228e | HESS J1507–622 | 3FHL | Disk | 0.362 | Ackermann et al. (2017) |
| J1514.2–5909e | MSH 15–52 | 3FHL | Disk | 0.243 | Ackermann et al. (2017) |
| J1533.9–5712e | HESS J1534–571 | New | Disk | 0.4 | Araya (2017) |
| J1552.4–5612e | MSH 15–56 PWN | New | Map | 0.08 | Devin et al. (2018) |
| J1552.9–5607e | MSH 15–56 SNR | New | Map | 0.3 | Devin et al. (2018) |
| J1553.8–5325e | FGES J1553.8–5325 | 3FHL | Disk | 0.523 | Ackermann et al. (2017) |

Table 4 continued on next page

Table 4 (continued)

| 4FGL Name | Extended Source | Origin | Spatial Form | Extent [deg] | Reference |
|---------------|-------------------|--------|--------------|---------------|---|
| J1615.3–5146e | HESS J1614–518 | 3FGL | Disk | 0.42 | Lande et al. (2012) |
| J1616.2–5054e | HESS J1616–508 | 3FGL | Disk | 0.32 | Lande et al. (2012) |
| J1626.9–2431e | FHES J1626.9–2431 | New | Gaussian | 0.29 | Ackermann et al. (2018) |
| J1631.6–4756e | FGES J1631.6–4756 | 3FHL | Disk | 0.256 | Ackermann et al. (2017) |
| J1633.0–4746e | FGES J1633.0–4746 | 3FHL | Disk | 0.61 | Ackermann et al. (2017) |
| J1636.3–4731e | SNR G337.0–0.1 | 3FHL | Disk | 0.139 | Ackermann et al. (2017) |
| J1642.1–5428e | FHES J1642.1–5428 | New | Disk | 0.696 | Ackermann et al. (2018) |
| J1652.2–4633e | FGES J1652.2–4633 | 3FHL | Disk | 0.718 | Ackermann et al. (2017) |
| J1655.5–4737e | FGES J1655.5–4737 | 3FHL | Disk | 0.334 | Ackermann et al. (2017) |
| J1713.5–3945e | RX J1713.7–3946 | 3FHL | Map | 0.56 | H. E. S. S. Collaboration et al. (2018) |
| J1723.5–0501e | FHES J1723.5–0501 | New | Gaussian | 0.73 | Ackermann et al. (2018) |
| J1741.6–3917e | FHES J1741.6–3917 | New | Disk | 1.65 | Ackermann et al. (2018) |
| J1745.8–3028e | FGES J1745.8–3028 | 3FHL | Disk | 0.528 | Ackermann et al. (2017) |
| J1801.3–2326e | W 28 | 2FGL | Disk | 0.39 | Abdo et al. (2010e) |
| J1804.7–2144e | HESS J1804–216 | 3FHL | Disk | 0.378 | Ackermann et al. (2017) |
| J1805.6–2136e | W 30 | 2FGL | Disk | 0.37 | Ajello et al. (2012) |
| J1808.2–2028e | HESS J1808–204 | New | Disk | 0.65 | Yeung et al. (2016) |
| J1810.3–1925e | HESS J1809–193 | New | Disk | 0.5 | Araya (2018b) |
| J1813.1–1737e | HESS J1813–178 | New | Disk | 0.6 | Araya (2018b) |
| J1824.5–1351e | HESS J1825–137 | 2FGL | Gaussian | 0.75 | Grondin et al. (2011) |
| J1834.1–0706e | SNR G24.7+0.6 | 3FHL | Disk | 0.214 | Ackermann et al. (2017) |
| J1834.5–0846e | W 41 | 3FHL | Gaussian | 0.23 | Abramowski et al. (2015) |
| J1836.5–0651e | FGES J1836.5–0651 | 3FHL | Disk | 0.535 | Ackermann et al. (2017) |
| J1838.9–0704e | FGES J1838.9–0704 | 3FHL | Disk | 0.523 | Ackermann et al. (2017) |
| J1840.8–0453e | Kes 73 | New | Disk | 0.32 | Li et al. (2017a) |
| J1840.9–0532e | HESS J1841–055 | 3FGL | 2D Gaussian | (0.62, 0.38) | Aharonian et al. (2008) |
| J1852.4+0037e | Kes 79 | New | Disk | 0.63 | Li et al. (2017a) |
| J1855.9+0121e | W 44 | 2FGL | 2D Ring | (0.30, 0.19) | Abdo et al. (2010f) |
| J1857.7+0246e | HESS J1857+026 | 3FHL | Disk | 0.613 | Ackermann et al. (2017) |
| J1908.6+0915e | SNR G42.8+0.6 | New | Disk | 0.6 | Li et al. (2017a) |
| J1923.2+1408e | W 51C | 2FGL | 2D Disk | (0.375, 0.26) | Abdo et al. (2009b) |
| J2021.0+4031e | γ -Cygni | 3FGL | Disk | 0.63 | Lande et al. (2012) |
| J2028.6+4110e | Cygnus X cocoon | 3FGL | Gaussian | 3.0 | Ackermann et al. (2011a) |
| J2045.2+5026e | HB 21 | 3FGL | Disk | 1.19 | Pivato et al. (2013) |
| J2051.0+3040e | Cygnus Loop | 2FGL | Ring | 1.65 | Katagiri et al. (2011) |
| J2129.9+5833e | FHES J2129.9+5833 | New | Gaussian | 1.09 | Ackermann et al. (2018) |
| J2208.4+6443e | FHES J2208.4+6443 | New | Gaussian | 0.93 | Ackermann et al. (2018) |
| J2301.9+5855e | CTB 109 | 3FHL | Disk | 0.249 | Ackermann et al. (2017) |
| J2304.0+5406e | FHES J2304.0+5406 | New | Gaussian | 1.58 | Ackermann et al. (2018) |

^aEmissivity model.

NOTE— List of all sources that have been modeled as spatially extended. The Origin column gives the name of the *Fermi*-LAT catalog in which that spatial template was introduced. The Extent column indicates the radius for Disk (flat disk) sources, the 68% containment radius for Gaussian sources, the outer radius for Ring (flat annulus) sources, and an approximate radius for Map (external template) sources. The 2D shapes are elliptical; each pair of parameters (a, b) represents the semi-major (a) and semi-minor (b) axes.

3.5. Limitations and Systematic Uncertainties

3.5.1. Diffuse emission model

The model of diffuse emission is the main source of uncertainties for faint sources. Contrary to the effective area, it does not affect all sources equally: its effects are smaller outside the Galactic plane where the diffuse emission is fainter and varying on larger angular scales. It is also less of a concern at high energy (> 3 GeV) where the core of the PSF is narrow enough that the sources dominate the background under the PSF. But it is a serious concern inside the Galactic plane at low energy (< 1 GeV) and particularly inside the Galactic ridge ($|l| < 60^\circ$) where the diffuse emission is strongest and very structured, following the molecular cloud distribution. It is not easy to assess precisely how large the uncertainties are, because they relate to uncertainties in the distributions of interstellar gas, the interstellar radiation field, and cosmic rays, which depend in detail on position on the sky.

We estimate, from the residuals over the entire Galactic plane, that the systematics are at the 3% level. This is already an achievement, but the statistical Poisson errors corresponding to the diffuse emission integrated over the PSF (as described in Appendix A) are much smaller than this. Integrating energies up to twice the current one in the Galactic ridge, the statistical precision is 0.2, 0.4, 1, 2, 5% above 100, 200, 500 MeV, 1, 2 GeV respectively.

The weights are able to mitigate the systematic effects globally, but cannot correct the model locally. In particular underestimating the mass of an interstellar cloud will always tend to create spurious sources on top of it, and overestimating diffuse emission at a particular place tends to make the sources on top of it harder than they should be (because the model creates negative residuals there, and those are felt mostly at low energy).

3.5.2. Analysis method

As in 3FGL, we use the *pointlike*-based method described in § 3.1 to estimate systematic errors due to the way the main *gtlike*-based method (§ 3.2) is set up in detail. Many aspects differ between the two methods: the code, the weights implementation, the RoIs, the diffuse model adjustments. The *pointlike*-based method does not remove faint sources (with $TS < 25$) from the model. Even the data differ, since the *pointlike*-based method uses *Front* and *Back* event types whereas the *gtlike*-based method uses PSF event types with a different zenith angle cut. Both methods reject a fraction of the events below 1 GeV, but not the same one.

Because of all those differences, we expect that comparing the results of the two methods source by source can provide an estimate of the sensitivity of the source list to details of the analysis. In particular we use it to flag sources whose spectral characterization differs a lot with the two methods (Flags 1 and 3 in Table 5).

3.5.3. Analysis Flags

As in 3FGL we identified a number of conditions that should be considered cautionary regarding the reality of a source or the magnitude of the systematic uncertainties of its measured properties. They are described in Table 5. Because this is a preliminary catalog a number of flags are unfilled (4, 5, 6, 7, 11).

In 4FGL 877 sources are flagged (about 17%): 207 sources were flagged with flag 1, 227 were flagged with flag 2, 333 were flagged with flag 3 (those three flags alert to a different result with *pointlike* or the previous diffuse model), 98 with flag 9 (bad localization), 35 with flag 10 (bad spectral representation) and 154 with flag 12 (highly curved).

Table 5. Definitions of the Analysis Flags

| Flag ^a | Meaning |
|-------------------|--|
| 1 | Source with $TS > 35$ which went to $TS < 25$ when changing the diffuse model (§ 3.5.1) or the analysis method (§ 3.5.2). Sources with $TS \leq 35$ are not flagged with this bit because normal statistical fluctuations can push them to $TS < 25$. |
| 2 | Moved beyond its 95% error ellipse when changing the diffuse model. |
| 3 | Flux (> 1 GeV) or energy flux (> 100 MeV) changed by more than 3σ when changing the diffuse model or the analysis method. Requires also that the flux change by more than 35% (to not flag strong sources). |
| 4 | Not used. |
| 5 | Not used. |
| 6 | Not used. |
| 7 | Not used. |
| 8 | Not used. |
| 9 | Localization Quality > 8 in <i>pointlike</i> (§ 3.1) or long axis of 95% ellipse $> 0^\circ.25$. |
| 10 | Spectral Fit Quality > 30 in <i>pointlike</i> . |
| 11 | Not used. |
| 12 | Highly curved spectrum; LP_beta fixed to 1 or PLEC_Index fixed to 0 (see § 3.3). |

^aIn the FITS version (Table 9 in Appendix B) the values are encoded as individual bits in a single column, with Flag n having value $2^{(n-1)}$.

Only 12% of the sources with power-law index $\Gamma < 2.5$ are flagged, but 34% of the soft sources with $\Gamma \geq 2.5$. This attests of the exacerbated sensitivity of soft sources to the underlying background emission. Only 10% of associated sources are flagged but 24% of the non-associated ones. This is in part because the associated sources tend to be brighter, therefore more robust, and also because many flagged sources are close to the Galactic plane where the association rate is low.

4. THE 4FGL CATALOG

4.1. Catalog Description

The catalog contains 5098 sources⁷. The source designation is 4FGL JHHMM.m+DDMM where the 4 indicates that this is the fourth LAT catalog, FGL represents *Fermi* Gamma-ray LAT. The 75 sources that were modeled as extended for 4FGL (§ 3.4) are singled out by an e appended to their names. The catalog columns are described in Appendix B. Figure 2 illustrates the distribution of the 4FGL sources over the sky, separately for extragalactic (blue) and Galactic (red) classes.

4.2. Comparison with 3FGL and earlier

4.2.1. General comparison

Figure 3 shows the energy flux distribution in 1FGL, 2FGL, 3FGL and 4FGL. Comparing the current flux threshold with those published in previous LAT Catalog papers we see that in 4FGL the threshold is down to $\simeq 2 \times 10^{-12}$ erg cm⁻² s⁻¹, quantifying the gain from 3FGL. Above 10^{-11} erg cm⁻² s⁻¹ the 2FGL and 3FGL distributions are entirely compatible with 4FGL. The 1FGL distribution shows a distinct bump between 1 and 2×10^{-11} erg cm⁻² s⁻¹. That accumulation of fluxes was clearly incorrect. We attribute it primarily to overestimating significances and fluxes due to the unbinned

⁷ The file has 5099 entries because the PWN component of the Crab nebula is represented by two cospatial sources (§ 3.3).

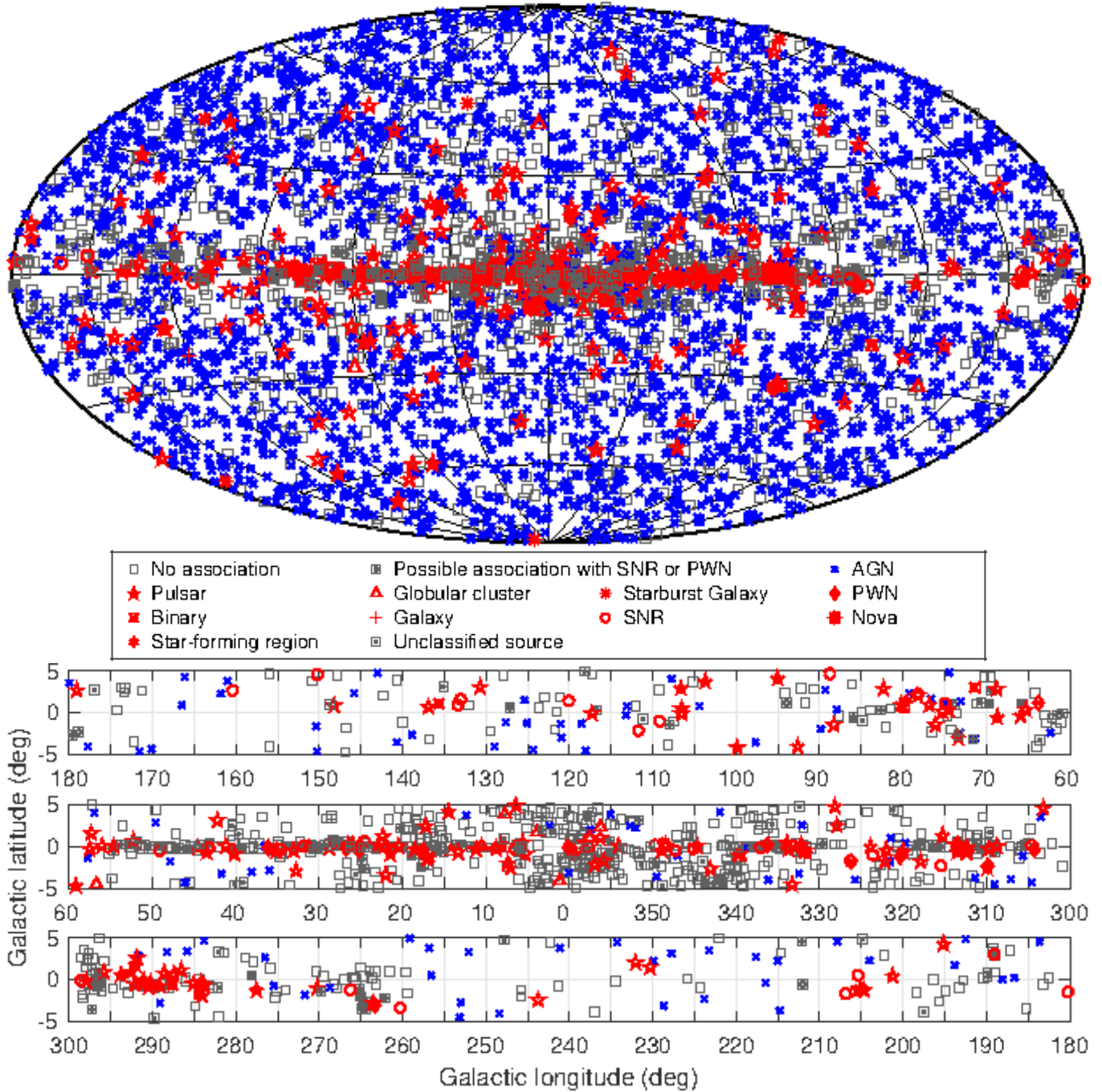


Figure 2. Full sky map (top) and blow-up of the Galactic plane split into three longitude bands (bottom) showing sources by source class (see Table 7, no distinction is made between associations and identifications). All AGN classes are plotted with the same blue symbol for simplicity. Other associations to a well-defined class are plotted in red. Unassociated sources and sources associated to counterparts of unknown nature are plotted in black.

likelihood bias in the 1FGL analysis, and also to the less accurate procedure then used to extract source flux (see discussion in the 2FGL paper).

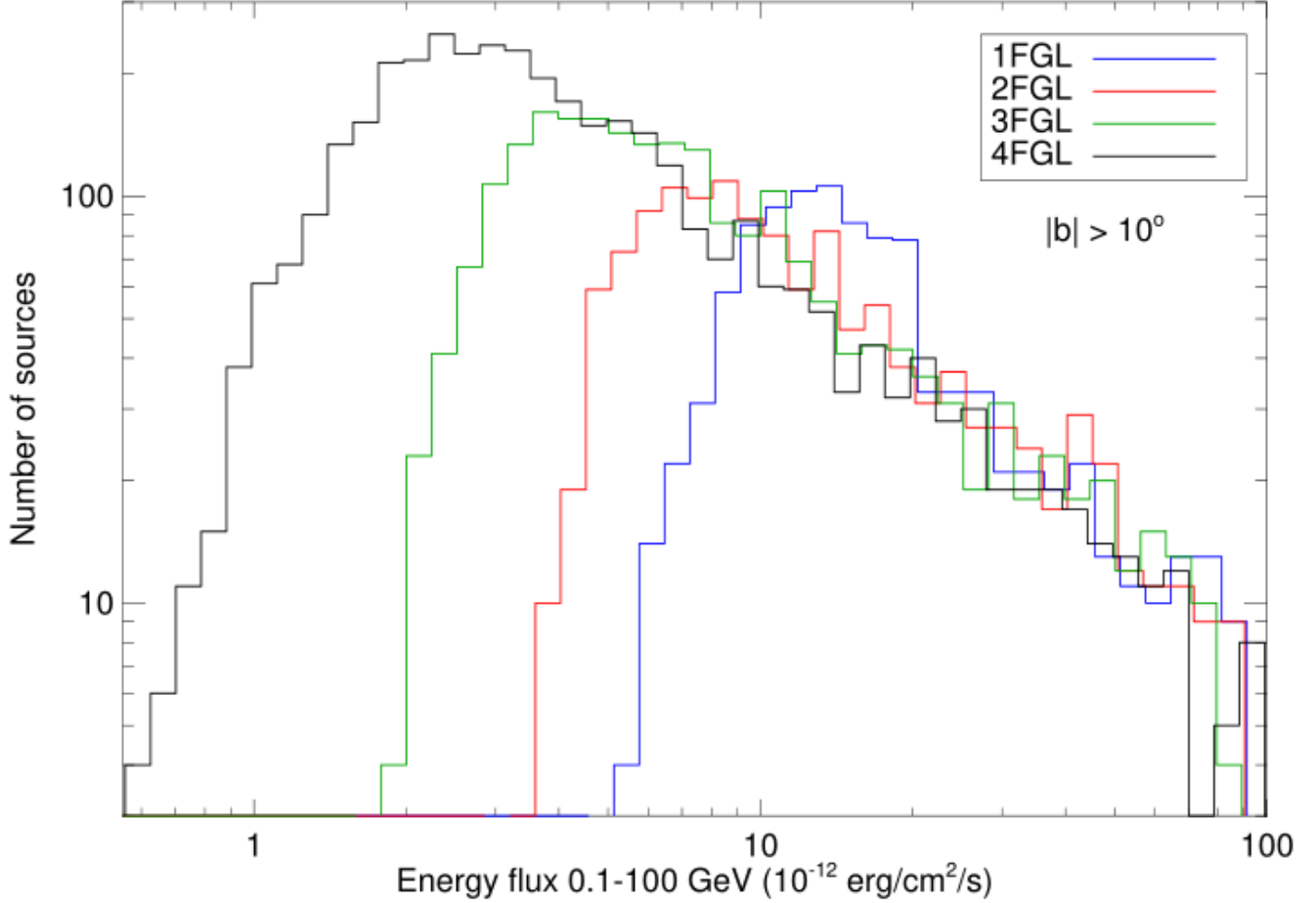


Figure 3. Distributions of the energy flux for the high-latitude sources ($|b| > 10^\circ$) in the 1FGL (1043 sources, blue), 2FGL (1319 sources, red), 3FGL (2193 sources, green) and 4FGL (3663 sources, black) catalogs, illustrating the approximate detection threshold.

The threshold at low flux is less sharp in 4FGL than it was in 2FGL or 3FGL. This reflects a larger dependence of the detection threshold on the power-law index. The detection threshold for soft sources decreases only slowly with exposure due to the weights (Appendix A).

The power-law index Γ is a way to compare all sources over all catalog generations, ignoring the complexities of the curved models. Figure 4 shows the four distributions of the power-law indices of the sources at high Galactic latitude are very similar. Their averages and widths are $\Gamma_{1\text{FGL}} = 2.22 \pm 0.33$, $\Gamma_{2\text{FGL}} = 2.17 \pm 0.30$, $\Gamma_{3\text{FGL}} = 2.22 \pm 0.31$ and $\Gamma_{4\text{FGL}} = 2.23 \pm 0.30$.

Small differences in the power-law index distributions could be related to slightly different systematic uncertainties in the effective area between the IRFs used respectively for 4FGL, 3FGL, 2FGL, and 1FGL (Table 1). There is actually no reason why the distribution should remain the same, since the detection threshold depends on the index and the log N-log S of flat-spectrum radio quasars, which are soft *Fermi* sources, differs from that of BL Lacs, which are hard in the *Fermi* band (Ackermann et al. 2015, Fig. 7). The apparent constancy may largely be the result of competing effects.

We have compared the distribution of error radii (defined as the geometric mean of the semi-major and semi-minor axes of the 95% confidence error ellipse) of the 1FGL, 2FGL, 3FGL and

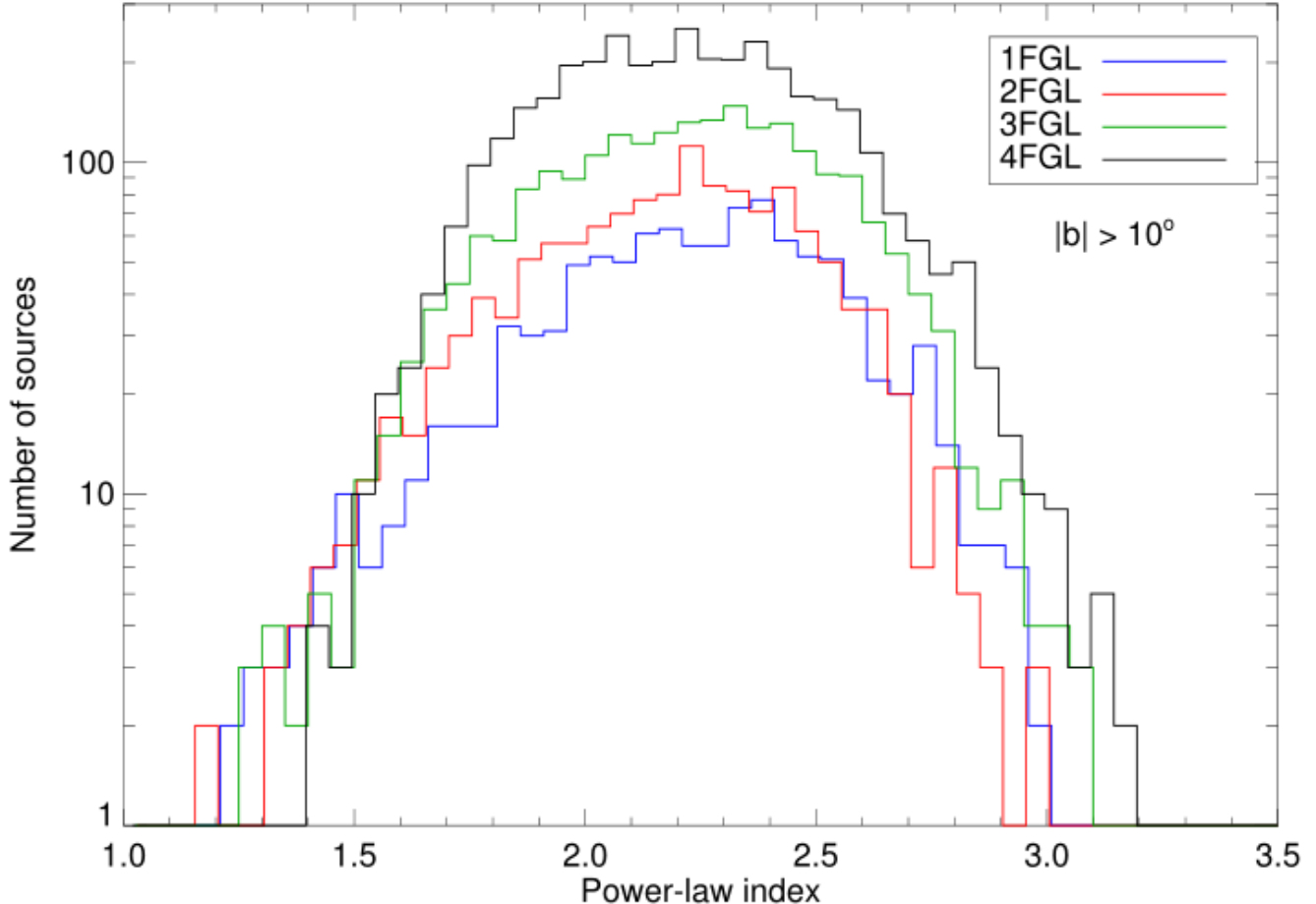


Figure 4. Distributions of the power-law index for the high-latitude sources in the 1FGL (blue), 2FGL (red), 3FGL (green) and 4FGL (black) catalogs. The sources are the same as in Fig 3.

4FGL sources at high Galactic latitude. Overall the source localization improves mechanically as more photons are added to previously detected sources. We concentrate instead on what happens specifically for faint sources. Figure 5 shows the distribution of 95% confidence error radii for those sources with $25 < TS < 100$ in any of the catalogs. The improvement at a given TS level is partly due to the event-level analysis (from Pass 6 to 7 and 8, see Table 1) and partly to the fact that, at a given significance level and for a given spectrum, fainter sources over longer exposures are detected with more photons. This improvement is key to preserving a high rate of source associations (§ 6) even though the source density increases.

4.2.2. Step-by-step from 3FGL to 4FGL

In order to understand the improvements of the 4FGL analysis with respect to 3FGL, we have considered the effects of changing the analysis and the data set without changing the time range (i.e., leaving it as four years). To that end we started with the same seeds as the 3FGL catalog, changed each element in sequence (in the order of the list below) and compared each intermediate result with the previous one. The effect of introducing energy dispersion was described in § 3.2.

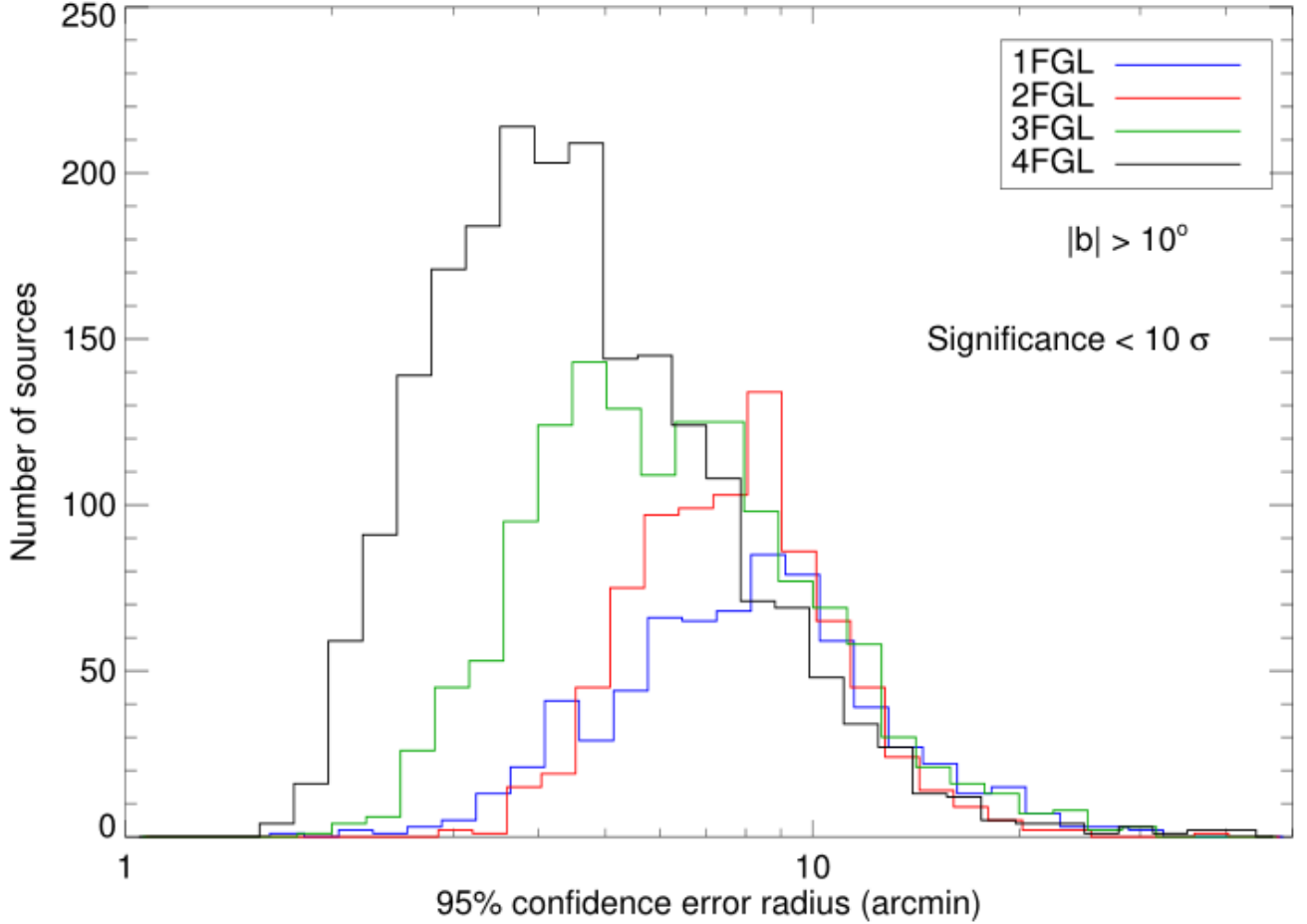


Figure 5. Distributions of the 95% confidence error radii for high-latitude sources with significance < 10 in 1FGL (713 sources, blue), 2FGL (843 sources, red), 3FGL (1387 sources, green) and 4FGL (2107 sources, black), illustrating the improvement of localizations for sources of equivalent detection significances.

- We first switched from P7REP to Pass 8, eliminating the Earth limb by cutting zenith angles $< 90^\circ$ at 100 to 300 MeV and $< 97.5^\circ$ at 300 MeV to 1 GeV for Front, $< 80^\circ$ at 100 to 300 MeV and $< 95^\circ$ at 300 MeV to 1 GeV for Back. The resulting TS increased by 27%, in keeping with the effective area increase (the number of sources at $TS > 25$ did not rise, for lack of seeds). Energy flux decreased by 7% in faint sources. In the Galactic plane sources softened by 0.04 on average. Both effects appear to be due to the diffuse emission modeling, because they are absent in the bright sources. The isotropic spectrum was recomputed, and even though the Galactic diffuse model was the same, its effects differed because the effective area increase with Pass8 is stronger at low energy. Those offsets are accompanied by a large scatter: only 72% of P7REP events are still in P8R3, and even for those the reconstructed direction differs.
- Switching from Front/Back to PSF event types increased TS by 10% (140 more sources). This was the intended effect (keep good events and bad ones apart as much as possible). No systematic effect was noted on energy flux. Soft sources got somewhat softer with PSF event types (power-law indices larger than 2.7 increased by 0.1 on average), but the bias averaged over

all sources was only +0.01. The number of curved sources decreased by 50 and the curvature β by 0.025 (this is the same effect: low energies moved up, so spectra got closer to a power law).

- Applying the weights results in a general decrease of TS and increase of errors, as expected. However, because source detection is dominated by energies above 1 GeV even without weights, the effect is modest (the number of sources decreased by only 40). The difference is of course largest for soft sources and in the Galactic plane, where the background is larger and the weights are smaller. There are a few other side effects. The number of curved sources went down by 30. This is because the lever arm is less as low energies have been played down. The pivot energy tended to go up for the same reason, and this resulted in a softening of the power-law index of curved sources (not exceeding 0.1). Overall in the Galactic ridge the power-law index increased by 0.025.

We evaluated the other two changes on eight years of data:

- Changing the energy range to start at 50 MeV did not improve TS , as expected (the PSF is too broad below 100 MeV to contribute to significance). The energy flux (defined in the same 100 MeV to 100 GeV band) tended to go down in the Galactic plane (by as much as -10% in the Galactic ridge) and the power-law index tended to become harder (by as much as -0.05 in the Galactic ridge). This is because the low-energy information tends to stabilize artificially soft sources. Neither effect was noticeable outside the Galactic plane. The other consequence was to increase the number of significantly curved sources by 80, because the broader energy range made it easier to detect curvature (this was true everywhere in the sky).
- Changing the Galactic diffuse emission model from `gll_iem_v06` used in 3FGL to that used here (§ 2.4), without changing the analysis or the data. The flags in § 3.5.3 are based on comparing to a version of the FLSY source list (using `gll_iem_v06`) extending the energy range to start at 50 MeV, but still differing from 4FGL in the extended sources and the energy bins in the first (50 – 100 MeV) component. Because of those differences the current flags are a little conservative. A detailed discussion of that effect is deferred to the full 4FGL release.

In conclusion, to first order the resulting net changes are not very large, consistent with the general comparison between 4FGL and 3FGL in § 4.2.1. Systematic effects are collectively visible but within calibration errors, and within statistical errors of individual sources.

5. AUTOMATED SOURCE ASSOCIATIONS

Table 6. Catalogs Used for the Automatic Source Association Methods

| Name | Objects ^a | Ref. |
|----------------------------|----------------------|--|
| High \dot{E}/d^2 pulsars | 313 | Manchester et al. (2005)^b |
| Other normal pulsars | 2248 | Manchester et al. (2005)^b |
| Millisecond pulsars | 240 | Manchester et al. (2005)^b |
| Pulsar wind nebulae | 69 | Collaboration internal |
| High-mass X-ray binaries | 137 | Chaty et al. (2018) |

Table 6 continued on next page

Table 6 (continued)

| Name | Objects ^a | Ref. |
|--|----------------------|---|
| Low-mass X-ray binaries | 187 | Liu et al. (2007) |
| Point-like SNR | 158 | Green (2014) ^c |
| Extended SNR ^f | 295 | Green (2014) ^c |
| Globular clusters | 160 | Harris (1996) |
| Dwarf galaxies ^f | 100 | McConnachie (2012) |
| Nearby galaxies | 276 | Schmidt et al. (1993) |
| IRAS bright galaxies | 82 | Sanders et al. (2003) |
| BZCAT (Blazars) | 3561 | Massaro et al. (2009) |
| BL Lac | 1371 | Véron-Cetty & Véron (2010) |
| AGN | 10066 | Véron-Cetty & Véron (2010) |
| QSO | 129,853 | Véron-Cetty & Véron (2010) |
| Seyfert galaxies | 27651 | Véron-Cetty & Véron (2010) |
| Radio loud Seyfert galaxies | 29 | Collaboration internal |
| Radio-loud Seyfert galaxies | 556 | Rakshit et al. (2017) |
| FRICAT (Radiogalaxies) | 233 | Capetti, A. et al. (2017a) |
| FRIICAT (Radiogalaxies) | 123 | Capetti, A. et al. (2017b) |
| Giant Radio Source | 349 | Kuźmicz et al. (2018) |
| 2WHSP | 1691 | Chang et al. (2017) |
| WISE blazar catalog | 12319 | D'Abrusco et al. (2014) |
| Radio Fundamental Catalog | 14786 | http://astrogeo.org/rfc |
| CGRaBS | 1625 | Healey et al. (2008) |
| CRATES | 11499 | Healey et al. (2007) |
| ATCA 20 GHz southern sky survey | 5890 | Murphy et al. (2010) |
| 105-month Swift/BAT catalog | 1632 | Oh et al. (2018) |
| 4 th IBIS catalog | 939 | Bird et al. (2016) |
| 1st AGILE catalog ^e | 54 | Pittori et al. (2009) |
| 3rd EGRET catalog ^e | 271 | Hartman et al. (1999) |
| EGR catalog ^e | 189 | Casandjian & Grenier (2008) |
| 0FGL list ^e | 205 | Abdo et al. (2009c, 0FGL) |
| 1FGL catalog ^e | 1451 | Abdo et al. (2010a, 1FGL) |
| 2FGL catalog ^e | 1873 | Nolan et al. (2012, 2FGL) |
| 3FGL catalog ^e | 3033 | Acero et al. (2015, 3FGL) |
| 1FHL catalog ^e | 514 | Ackermann et al. (2013, 1FHL) |
| 2FHL catalog ^e | 360 | Ackermann et al. (2016b, 1FHL) |
| 3FHL catalog ^e | 1556 | Ajello et al. (2017, 1FHL) |
| TeV point-like source catalog ^e | 108 | http://tevcat.uchicago.edu/ |
| TeV extended source catalog ^f | 72 | http://tevcat.uchicago.edu/ |
| LAT pulsars | 234 | Collaboration internal ^d |
| LAT identified | 145 | Collaboration internal |

Table 6 continued on next page

Table 6 (*continued*)

| Name | Objects ^a | Ref. |
|------|----------------------|------|
|------|----------------------|------|

^aNumber of objects in the catalog.

^bversion 1.56, <http://www.atnf.csiro.au/research/pulsar/psrcat>

^cGreen D. A., 2017, ‘A Catalogue of Galactic Supernova Remnants (2017 June version)’, Cavendish Laboratory, Cambridge, United Kingdom (available at <http://www.mrao.cam.ac.uk/surveys/snrs/>)

^d<https://confluence.slac.stanford.edu/display/GLAMCOG/Public+List+of+LAT-Detected+Gamma-Ray+Pulsars>

^eFor these catalogs, the association is performed by requiring that the separation from the 4FGL sources is less than the quadratic sum of the 99.9% confidence error radii.

^fFor these catalogs of extended sources, the association is performed by requiring that the separation from the 4FGL sources is less than the quadratic sum of the 95% confidence error radii.

The Bayesian method (Abdo et al. 2010a) for the *Fermi*-LAT, implemented with the *gtsrcid* tool⁸, was developed following the prescription devised by Mattox et al. (1997) for EGRET. It relies on the fact that the angular distance between a LAT source and a candidate counterpart is driven by i) the position uncertainty in the case of a real association ii) the counterpart density in the case of a false (random) association. In addition to the angular-distance probability density functions for real and false associations, the posterior probability depends on a prior. This prior is calibrated via Monte Carlo simulations so that the number of false associations, N_{false} is equal to the sum of the association-probability complements. For a given counterpart catalog, the so-obtained prior is found to be close to N_{assoc}/N_{tot} , where N_{assoc} is the number of associations from this catalog and N_{tot} is the number of catalog sources. The sum of the association probabilities over all pairs (γ -ray source, potential counterpart) gives the total number of real associations for a particular catalog. The total numbers of associations are reported below for the various classes, where the overlap between associations from different catalogs is taken into account. A uniform threshold of 0.8 is applied to the posterior probability for the association to be retained. The reliability of the Bayesian associations is assessed by verifying that the distribution of the angular offset between γ -ray source and counterpart matches well the expected one in the case of a true association, i.e., a Rayleigh function with its width parameter given by the sources positional uncertainties.

The list of counterpart catalogs, listed in Table 6, includes known γ -ray-emitting source classes: Active Galactic Nuclei (AGN, Ackermann et al. (2015)), galaxies (Abdo et al. 2010g), pulsars (Abdo et al. 2013), pulsar-wind nebulae (Ackermann et al. 2011c), supernova remnants (Acero et al. 2016c), globular clusters (Abdo et al. 2010h), low- and high-mass X-ray binaries (Abdo et al. 2010i, 2009d) or surveys of candidate blazars at other frequencies (radio, IR, X-rays). The reported source classes are derived in the same way as in 3FGL. For non-AGN sources, this classification is based on the nature of the association catalogs. For AGN, the subclasses as flat-spectrum radio quasars (FSRQ), BL Lac-type objects (BLL), blazar candidates of uncertain type (BCU), radio galaxies (RDG), narrow-line Seyfert 1 (NLSY1), steep spectrum radio quasar (SSRQ), Seyfert galaxies (SEY) or simply AGN (if no other particular subclass can be assigned), have been selected according to the counterpart properties at other wavelengths. Please note that we did not use the blazar classes from the Simbad database

⁸ <https://fermi.gsfc.nasa.gov/ssc/data/analysis/scitools/overview.html>

⁹ since some of them correspond to predictions based on the WISE-strip approach (D’Abrusco et al. 2014) and not to assessment with the measured strengths of the emission lines.

In complement to the Bayesian method, the Likelihood-Ratio (LR) method (Ackermann et al. 2011b, 2015), following de Ruiter et al. (1977) provides supplementary associations with blazar candidates based on large radio and X-ray surveys: NVSS (Condon et al. 1998), SUMSS (Mauch et al. 2003), ROSAT (Voges et al. 1999, 2000) and AT20G (Murphy et al. 2010). This method is similar in essence to the Bayesian method but the false association rate is derived from the density of objects brighter than the considered candidate, assessed from the survey log N-log S distribution. While the LR method is able to handle large surveys, its fraction of false associations is notably larger than in the Bayesian method (typically 10% vs 2%). The overlap between the results of the Bayesian and LR methods is about 75% for blazars. Because the surveys include a large number of Galactic sources at low Galactic latitudes, the class of $|b| < 10^\circ$ sources associated solely via the LR-method has been set to ‘UNK’ (standing for unknown) as opposed to the ‘BCU’ class used by default for sources at larger latitudes.

The cross-correlation with previous γ -ray catalogs has been performed by requiring that the 99.9% ellipse regions overlap (using $r_{99.9}/r_{95}=1.52$). Firm identifications are based on periodic variability for LAT-detected pulsars or X-ray binaries, correlated variability at other wavelengths for AGN or spatial morphology related to that found in another band for extended sources.

6. ASSOCIATION SUMMARY

The association summary is given in table 7. Out of 5099 LAT sources in 4FGL, 1525 are unassociated (30%) or classified as “SPP” or as “unknown” (4% in total). Some 3257 sources are associated with the Bayesian method (909 associations from this method only, overall $N_{false}=35.6$), 2612 sources with the LR method (264 associations from this method only, $N_{false}=27.9$ for the latter). The overall association fraction, 70%, is similar to that obtained in previous LAT catalogs. It must be noted that the association fraction is lower for fainter sources (all bright sources are associated), in particular due to their larger error regions. This fraction also drops as sources lie closer to the Galactic plane as illustrated in Figure 6. It decreases from about 85% at high Galactic latitudes to $\simeq 40\%$ close to the Galactic plane. The reason for such an effect is twofold. First, the number of unassociated Galactic sources is large. Secondly, the flux limits of the extragalactic-counterpart catalogs are larger due to extinction effects in these directions. The properties of the unassociated sources are discussed below.

Sources reported as new below mean that they were not in previous FGL catalogs, although their detections may have been reported in other works, e.g., Arsioli & Polenta (2018); Zhang et al. (2016), or in specialized LAT catalogs.

6.1. Extragalactic sources

6.1.1. Active Galactic Nuclei

The largest source population in 4FGL is that of AGN, with 2938 blazars, 38 radio galaxies and 33 other AGN. The blazar sample comprises 681 flat-spectrum radio quasars (FSRQ), 1102 BL Lac-type objects (BL Lac) and 1152 blazar candidates of unknown type (BCU) The detailed properties of the 4FGL AGN, including redshifts and fitted synchrotron-peak positions, will be the subject of the 4LAC companion catalog. We note here that the relative separation in γ -ray spectral hardness

⁹ <http://simbad.u-strasbg.fr/simbad/>

Table 7. LAT 4FGL Source Classes

| Description | Identified | | Associated | |
|--|------------|--------|------------|--------|
| | Designator | Number | Designator | Number |
| Pulsar, identified by pulsations | PSR | 231 | ... | ... |
| Pulsar, no pulsations seen in LAT yet | ... | ... | psr | 10 |
| Pulsar wind nebula | PWN | 12 | pwn | 6 |
| Supernova remnant | SNR | 24 | snr | 16 |
| Supernova remnant / Pulsar wind nebula | SPP | 0 | spp | 92 |
| Globular cluster | GLC | 0 | glc | 30 |
| Star-forming region | SFR | 3 | sfr | 0 |
| High-mass binary | HMB | 5 | hmb | 3 |
| Low-mass binary | LMB | 1 | lmb | 1 |
| Binary | BIN | 1 | bin | 0 |
| Nova | NOV | 1 | nov | 0 |
| BL Lac type of blazar | BLL | 22 | bll | 1080 |
| FSRQ type of blazar | FSRQ | 42 | fsrq | 639 |
| Radio galaxy | RDG | 6 | rdg | 32 |
| Non-blazar active galaxy | AGN | 1 | agn | 16 |
| Steep spectrum radio quasar | SSRQ | 0 | ssrq | 2 |
| Compact Steep Spectrum radio source | CSS | 0 | css | 5 |
| Blazar candidate of uncertain type | BCU | 3 | bcu | 1152 |
| Narrow line Seyfert 1 | NLSY1 | 3 | nlsy1 | 5 |
| Seyfert galaxy | SEY | 0 | sey | 1 |
| Starburst galaxy | SBG | 0 | sbg | 7 |
| Normal galaxy (or part) | GAL | 2 | gal | 2 |
| Unknown | UNK | 0 | unk | 118 |
| Total | ... | 357 | ... | 3217 |
| Unassociated | ... | ... | ... | 1525 |

NOTE—The designation ‘spp’ indicates potential association with SNR or PWN. Designations shown in capital letters are firm identifications; lower case letters indicate associations.

between FSRQs and BL Lacs already reported in previous LAC AGN catalogs is confirmed: 93% of FSRQs and 81% of BL Lacs have power-law photon indices greater and lower than 2.2 respectively. Among the 71 non-blazar AGN, 36 were present in the 3FGL. The 16 new radio galaxies are: 3C 120, NGC 315, CRATES J070908.00+483655, NGC 3894, TXS 1303+114, B2.2 1447+27, PKS 1514+00, TXS 1516+064, PKS B1518+045, PKS 1839–48, PKS 2153–69, PKS 2225–308, PKS 2300–18, PKS 2324–02, PKS 2327–215, PKS 2338–295. Four 3FGL sources have changed classes to radio galaxies, all former bcu (TXS 0149+710, IC 4516, PKS 1304–215, CGCG 050–083) and one is missing: Cen B. The 33 ‘other AGN’ sources include five compact steep spectrum radio sources (CSS, three are new: 3C 138, 3C 216, 3C 309.1), two steep spectrum radio quasars (SSRQ, new is 3C 212), 8 Narrow-line Seyferts 1 (NLSY1), one Seyfert galaxy (Circinus, SEY) and 17 AGN of other types (AGN). Three NLSY1 are new: IERS B1303+515, B3 1441+476, TXS 2116–077.

6.1.2. Other galaxies

No other nearby galaxies, besides the SMC, LMC, and M 31, are detected. Seven starburst galaxies in the IRAS catalog (Sanders et al. 2003) are associated with 4FGL sources. Two sources, Arp 220 (Peng et al. 2016; Griffin et al. 2016; Yoast-Hull et al. 2017) and NGC 2146 (Tang et al. 2014), have

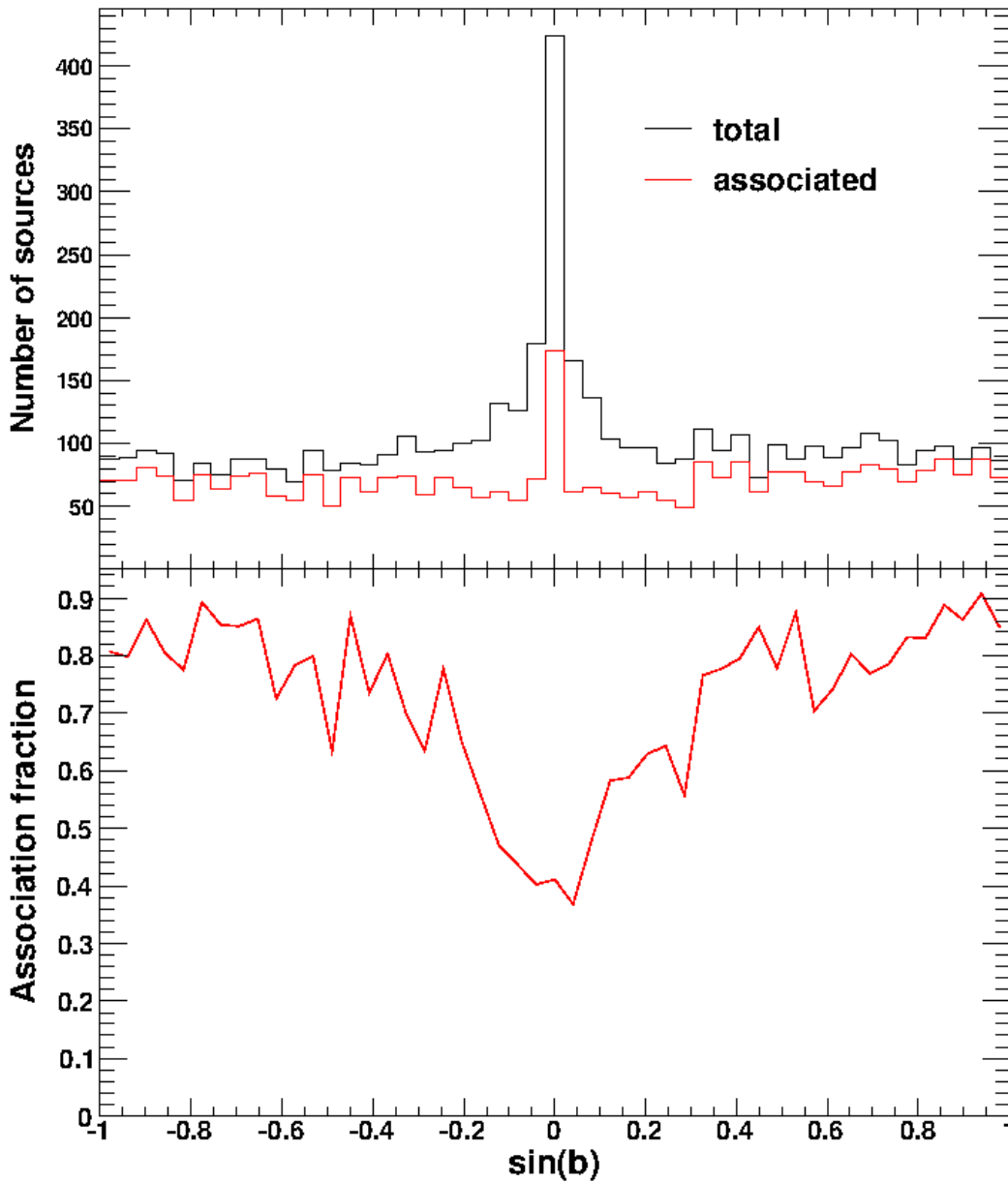


Figure 6. Upper panel: Distributions in Galactic latitude b of 4FGL sources (black histogram) and associated sources (blue histogram). Lower panel: Association fraction as a function of Galactic latitude.

been reported as LAT detections since the 3FGL release. [Yoast-Hull et al. \(2017\)](#) found an excess of γ rays over the expected starburst contribution in Arp 220, similar to the case of the Circinus galaxy ([Hayashida et al. 2013](#)). NGC 2146 being close ($0^{\circ}1$) to the FSRQ 1REX J061757+7816.1, the association is ambiguous. We favor the NGC 2146 association as no evidence for variability is found and the 4FGL photon index (2.16) is somewhat low for a FSRQ. Another source, NGC 3424, was not present in 3FGL. The IRAS source UGC 11041, which could have been classified as sbg shows significant variability in the LAT band, so the γ -ray emission most likely arises from an AGN (there is a flat-spectrum radio source, MG2 J175448+3442 at a distance of $2.4'$) and it is classified as

such. In addition to these seven associations, the Bayesian method predicts that three more 4FGL sources should be starburst galaxies. Some 4FGL sources are positionally consistent with known galaxy clusters, but these clusters host radio galaxies which are the most likely emitters. No dwarf galaxies have been detected.

6.2. Galactic sources

The Galactic sources include:

- 241 pulsars (PSR). The public list of LAT-detected pulsars is regularly updated¹⁰. Some 231 pulsars in this list are included in 4FGL (67 would have been missed by the association pipeline using the ATNF catalog), while 4 are absent because they did not pass the $TS > 25$ criterion. These pulsars represent by far the largest population of identified sources in 4FGL. Another 10 pulsars from the ATNF database are associated with 4FGL sources with high-confidence via the Bayesian method. This method predicts that about 30 extra 4FGL sources are ATNF pulsars. Note that out of the 24 pulsar candidates presented in 3FGL, pulsations have now been detected for 18 of them. The other 6 are not associated with pulsars in 4FGL anymore.
- 40 supernova remnants (SNR). Out of them, 24 are extended and thus firmly identified. The other 16 are not resolved. SNR G150.3+4.5 having a logp-normal spectral shape with a very hard photon index, Γ of 1.6 indicates that the emission is most likely leptonic and makes this source an excellent candidate for the Cherenkov Telescope Array (CTA). In contrary, the softer spectrum of SNR N132D (photon index=2.07) makes the hypothesis of a dominant hadronic emission likely. The significant spectral curvature seen in Puppis A is in accord with its non-detection in the TeV domain.
- 18 pulsar wind nebulae (PWN), 15 of them being extended. New additions are N 157B, PWN G63.7+1.1, HESS J1356–645, FGES J1631.6–4756, FGES J1836.5–0651, FGES J1838.9–0704, HESS J1857+026. The median photon index of the 4FGL PWN is 2.31. N 157B, located in LMC, has a photon index of 2.0, hinting at an additional contribution from a (yet-undetected pulsar at low energy on top of the PWN).
- 92 sources (referred to as SPP) of unknown nature but overlapping with known SNR or PWN and thus candidates to these classes. The estimation of missed associations of SNR, PWNe and SPP sources is made difficult by the intrinsic spatial extension of the sources; no attempts have thus been made along this line.
- 30 globular clusters (GLC). Missing relative to 3FGL is 2MS-GC01. The 16 new associations are NGC 362, NGC 1904, NGC 5286, NGC 5904, NGC 6139, NGC 6218, NGC 6304, NGC 6341, Terzan 2, Terzan 1, NGC 6402, NGC 6397, GLIMPSE02, GLIMPSE01, NGC 6838, NGC 7078. Only 2 extra 4FGL sources are estimated to be globular clusters.
- Six high-mass X-ray binaries (HMB). The three new sources are HESS J0632+057, which has a reported LAT detection after the 3FGL (Li et al. 2017b), RX J0648.0–4418/HD 49798, which is a peculiar X-ray binary (Mereghetti et al. 2011; Popov et al. 2018), and Cyg X-1,

¹⁰ See <https://confluence.slac.stanford.edu/display/GLAMCOG/Public+List+of+LAT-Detected+Gamma-Ray+Pulsars>

an archetypical black-hole binary reported after the 3FGL (Zdziarski et al. 2017; Zanin et al. 2016). Three extra 4FGL sources are estimated to be HMB according to the Bayesian method.

- Three star-forming regions; new since 3FHL is the association of the extended source FHES J1626.9–2431 (§ 3.4) with the ρ Ophiuchi star-forming region.
- Two low-mass X-ray binaries (LMB). PSR J1023+0038 is a known binary MSP/LXB transition system, with a change in γ -ray flux detected (Stappers et al. 2014) simultaneously with a state change, and was previously detected as 2FGL J1023.6+0040 (but not detected in the 3FGL). The LMB 2S 0921–630 (V395 Car) is a well-studied binary involving a neutron star and a K0 III star with an orbital period of 9 days (Shahbaz & Watson 2007) and is a new LAT detection.
- One binary star (BIN), η Carinae.
- One nova, V5668 Sagittarii. Other novae detected by the LAT are missing. Novae have short durations, and most are below the significance threshold because their signal is diluted over the eight years of 4FGL data.

6.3. Unassociated sources

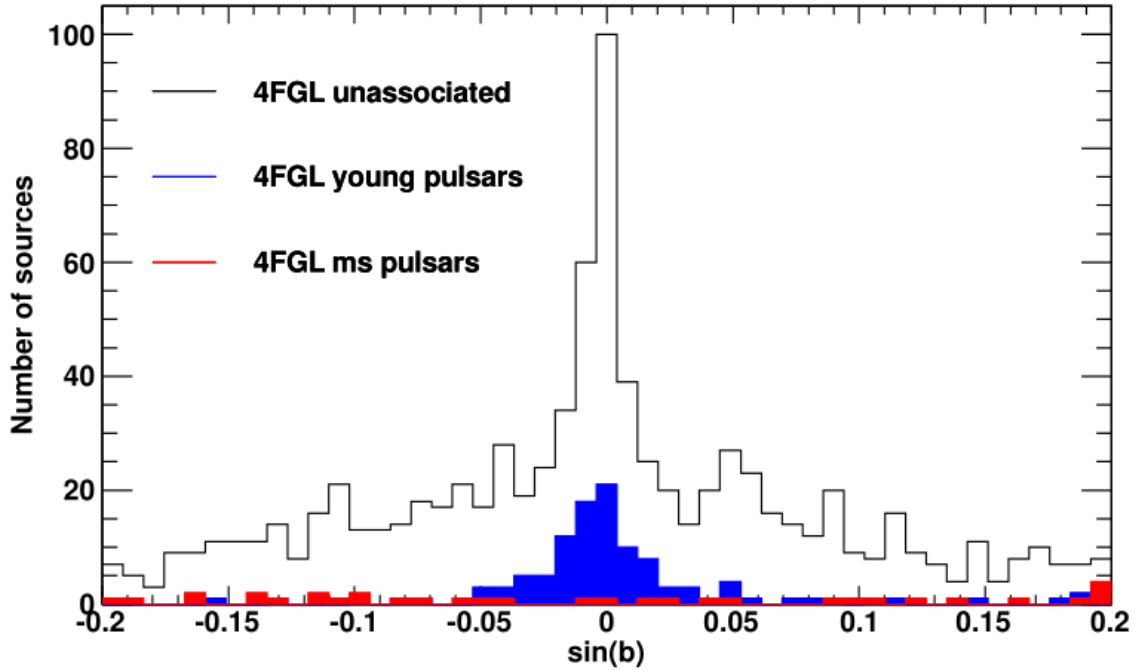


Figure 7. Distributions in Galactic latitude b of 4FGL unassociated sources (black histogram) compared to those of LAT-detected pulsars (young pulsars: blue histogram, millisecond pulsars: red histogram).

Out of the 1528 sources unassociated in 4FGL, 376 already present in 3FGL had no associations there. Another 32 sources previously associated in 3FGL have now lost their associations because of a shift in their locations relative to 3FGL.

About half of the unassociated sources are located less than 10° away from the Galactic plane. Their wide latitude extension is hard to reconcile with those of known classes of Galactic γ -ray sources. For

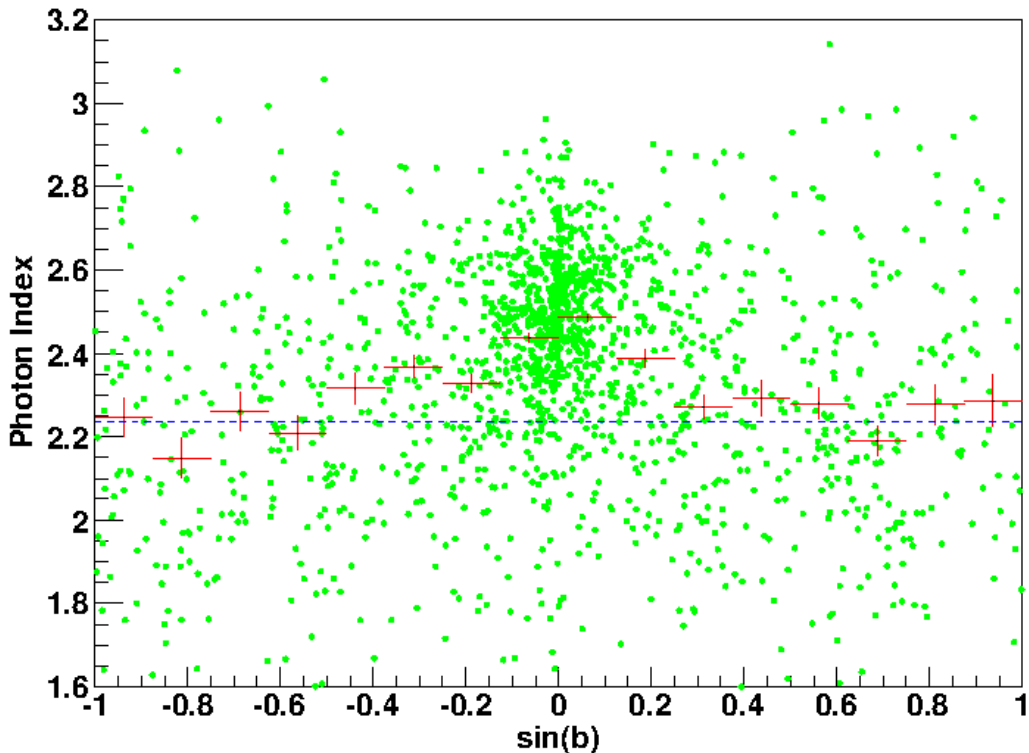


Figure 8. Green symbols: Power-law photon index versus Galactic latitude, b , for the unassociated 4FGL sources. Red bars: average photon index for different bins in b . Dashed blue line: average photon index of 4FGL BCU blazars.

instance, Figure 7 compares this latitude distribution with that of LAT pulsars. In addition to nearby millisecond pulsars, which have a quasi isotropic distribution, the LAT detects only young isolated pulsars (age $< 10^6$ y) which are by nature clustered close to the plane. Older pulsars, which have had time to drift further off the plane, show a wider Galactic-latitude distribution, more compatible with the observed distribution of the unassociated sources, but these pulsars have crossed the ‘ γ -ray death line’ and are hence undetectable. Attempts to spatially cross correlate the unassociated population with other potential classes, e.g., LXMB (Liu et al. 2007), O stars¹¹, B stars¹² have been unsuccessful. The observed clustering of these unassociated sources in high-density ‘hot spots’ may be a clue that they actually correspond to yet-to-be identified, relatively nearby extended sources. The Galactic latitude distribution near the plane is clearly non-gaussian as visible in Figure 7, which may indicate the presence of several components.

The spectral properties of these sources as well can provide insight into their nature, as illustrated in Figure 8 showing the power-law photon index versus the Galactic latitude. The change in spectral hardness with sky location demonstrates the composite nature of the unassociated population. The high-latitude sources shows an average photon index compatible with that of blazars of unknown type ($\Gamma=2.24$), a hint that these sources could predominantly be blazars. Unassociated sources lying closer

¹¹ GOSC <https://gosc.cab.inta-csic.es/>

¹² BeSS <http://basebe.obspm.fr/basebe/>

to the Galactic plane have softer spectra, closer to that expected of young pulsars ($\Gamma=2.42$). Another interesting possibility is that some of these unassociated sources actually correspond to WIMP dark matter annihilating in Galactic subhalos (Ackermann et al. 2012d; Coronado et al. 2019). Indeed, Λ CDM cosmology predicts the existence of thousands of them below $\sim 10^7 M_\odot$, i.e., not massive enough to retain gas or stars at all. As a result, they are not expected to emit at other wavelengths and therefore they would not possess astrophysical counterparts. Interestingly, this dark matter annihilation may yield a pulsar-like spectrum (?).

6.4. Sources missing from previous catalogs

Out of 3033 3FGL sources, 406 are missing in 4FGL for various reasons, including the change of diffuse emission model, point sources being absorbed into new extended ones or variability effects. Most of these missing sources had low significance in 3FGL. Only 74 sources were associated. The majority are blazars (32 BCU, 15 FSRQ, 1 BLL and 1 SSRQ) plus one AGN. It is remarkable that while BLL are 36% more numerous relative to FSRQ in 3FGL, a much lower fraction (by a factor of 20) has gone away in 4FGL, an effect possibly related to the larger variability of FSRQ relative to BLL observed in the LAT energy band (Ackermann et al. 2015). Other missing sources include 19 SPP, 3 PSR and one PWN. The nova V407 Cyg is now missing as it no longer fulfills the average-significance criterion.

Concerning sources missing from 3FHL, established with the same data set, they amount to 30, with 14 unassociated, 10 blazars (4 BLL and 6 BCU), 1 AGN, 4 ‘unknown’ and the HMB PSR B1259–63. All these sources had a TS close to the TS=25 significance threshold.

6.5. TeV sources

Table 8. Associations of 4FGL with Extended TeV Sources

| TeVCat Name ^a | 4FGL Name |
|--------------------------|----------------------------|
| Boomerang | J2229.0+6114 |
| CTA 1 | J0007.0+7303 |
| CTB 37A | J1714.4–3830 |
| CTB 37B | J1714.1–3811 |
| Crab | J0534.5+2201e |
| G318.2+00.1 | J1453.4–5858 |
| Geminga | J0633.9+1746 |
| HESS J1018–589 B | J1016.3–5857 |
| HESS J1026–582 | J1028.5–5819 |
| HESS J1303–631 | J1303.0–6312e |
| HESS J1356–645 | J1355.2–6420e |
| HESS J1420–607 | J1420.3–6046e |
| HESS J1427–608 | J1427.8–6051 |
| HESS J1458–608 | J1456.7–6050, J1459.5–6053 |
| HESS J1507–622 | J1507.9–6228e |
| HESS J1534–571 | J1533.9–5712e |
| HESS J1614–518 | J1615.3–5146e |
| HESS J1616–508 | J1616.2–5054e |
| HESS J1632–478 | J1633.0–4746e |
| HESS J1640–465 | J1640.6–4632 |

Table 8 continued on next page

Table 8 (*continued*)

| TeVcat Name ^a | 4FGL Name |
|--------------------------|--|
| HESS J1702–420 | J1705.7–4124 |
| HESS J1718–385 | J1718.2–3825 |
| HESS J1729–345 | J1730.1–3422 |
| HESS J1745–303 | J1745.8–3028e |
| HESS J1800–240 A | J1801.8–2358 |
| HESS J1800–240B | J1800.2–2403 , J1800.7–2355 , J1800.9–2407 |
| HESS J1804–216 | J1804.7–2144e |
| HESS J1808–204 | J1808.2–2028e |
| HESS J1809–193 | J1810.3–1925e |
| HESS J1813–126 | J1813.4–1246 |
| HESS J1813–178 | J1813.1–1737e |
| HESS J1825–137 | J1824.5–1351e |
| HESS J1826–130 | J1826.1–1256 |
| HESS J1834–087 | J1834.5–0846e |
| HESS J1841–055 | J1840.9–0532e |
| HESS J1848–018 | J1847.2–0141, J1848.6–0202, J1848.7–0129 |
| HESS J1857+026 | J1857.7+0246e |
| HESS J1858+020 | J1858.3+0209 |
| HESS J1912+101 | J1911.7+1014, J1912.7+0957, J1913.3+1019 |
| IC 443 | J0617.2+2234e |
| Kookaburra (Rabbit) | J1417.7–6057, J1418.7–6057 |
| Kookaburra PWN | J1420.0–6048 |
| MGRO J1908+06 | J1906.2+0631, J1907.9+0602 |
| MGRO J2031+41 | J2028.6+4110e |
| MSH 15–52 | J1514.2–5909e |
| RCW 86 | J1443.0–6227e |
| RX J0852.0–4622 | J0851.9–4620e |
| RX J1713.7–3946 | J1713.5–3945e |
| SNR G292.2–00.5 | J1119.1–6127 |
| TeV J1626-490 | J1628.2-4848 |
| Terzan 5 | J1748.0–2446 |
| VER J2019+407 | J2021.0+4031e |
| Vela X | J0833.1-4511e |
| W 28 | J1801.3–2326e |
| W 51 | J1923.2+1408e |
| Westerlund 1 | J1645.8–4533, J1648.4–4611, J1649.2–4513, J1650.3–4600, J1652.2–4516 |
| Westerlund 2 | J1023.3–5747e |

^aFrom <http://tevcat.uchicago.edu>.

The synergy between the LAT and the Cherenkov telescopes operating in the TeV energy domain has proven extremely fruitful, in particular by bringing out promising TeV candidates in the LAT catalogs. This approach, further motivated by the upcoming deployment of the Cherenkov Telescope Array, has justified the release of LAT source catalogs above 10 GeV, like the 3FHL (Ajello et al. 2017) based on 7 years of data. The associations of 4FGL sources with extended sources listed in TeVcat¹³ are presented in Table 8. Relative to 3FHL, 9 new extended TeV sources are associated

¹³ <http://tevcat.uchicago.edu/>

with 4FGL extended sources (TeV sources: HESS J1534–571, HESS J1808–204, HESS J1809–193, see § 3.4), or (sometimes multiple) 4FGL point sources (TeV sources: HESS J1718–385, HESS J1729–345, HESS J1848–018, HESS J1858+020, MGRO J1908+06, HESS J1912+101). All TeV blazars have 4FGL counterparts. The median value of Γ for 4FGL point sources associated with TeV point sources is 1.95, indicating hard spectra as expected. In associations with extended TeV sources, the median Γ changes from 2.09 to 2.38 depending on whether the 4FGL sources are extended or not. This fairly large difference favors the interpretation that most associations between extended TeV sources and non-extended 4FGL sources are accidental.

6.6. Counterpart positions

Whenever a high-confidence association with a point-like counterpart is obtained, we provide the most accurate counterpart position available and its uncertainty. In particular, 2277 4FGL AGN have Very Long Baseline Interferometry (VLBI) counterparts. VLBI, i.e., radio interferometry with baseline lengths of >1000 km is sensitive to radio emission from compact regions of AGN that are smaller than 20 mas, which corresponds to parsec scales. Such observations allow the determination of positions of the AGN jet base with milliarcsecond level accuracy. We used the Radio Fundamental Catalog¹⁴ based on the dedicated on-going observing program (Schinzel et al. 2015, 2017) with the Very Long Baseline Array (Napier et al. 1994), as well as VLBI data under other programs. The association between γ -ray source and VLBI counterpart was carried out along a similar, but distinct, scheme as that presented in § 5. This scheme (see Petrov et al. (2013) for more details) is based on the strong connection between the γ -ray emission and radio emission at parsec scales and on the sky density of bright compact radio sources being relatively low. The chance to find a bright background, unrelated compact radio source within the LAT positional error ellipse is low enough to establish association. The likelihood ratio (with a somewhat different definition from that implemented in the LR-method) was required to be greater than 8 to claim an association, with an estimated false association fraction of 1%.

For AGN without VLBI counterparts, the position uncertainties were set to typical values of 20'' for sources associated from the RASS survey and 10'' otherwise. For identified pulsars, the position uncertainties come from the rotation ephemeris used to find γ -ray pulsations, many of which were obtained from radio observations (Smith et al. 2019). If the ephemeris does not include the uncertainties and for pulsar candidates, we use the ATNF psrcat values. If neither of those exist, we use the 0.1° uncertainties from the list maintained by the WVU Astrophysics group¹⁵. Ephemeris position uncertainties are often underestimated, so we arbitrarily apply a minimum uncertainty of 1 mas. For globular clusters from Harris (1996), the position uncertainties were assigned a typical value of 2''¹⁶.

The *Fermi* LAT Collaboration acknowledges generous ongoing support from a number of agencies and institutes that have supported both the development and the operation of the LAT as well as scientific data analysis. These include the National Aeronautics and Space Administration and the Department of Energy in the United States, the Commissariat à l’Energie Atomique and the Centre National de la Recherche Scientifique / Institut National de Physique Nucléaire et de Physique des

¹⁴ Available at <http://astrogeo.org/rfc>

¹⁵ <http://astro.phys.wvu.edu/GalacticMSPs/GalacticMSPs.txt>

¹⁶ <https://heasarc.gsfc.nasa.gov/w3browse/all/globclust.html>

Particules in France, the Agenzia Spaziale Italiana and the Istituto Nazionale di Fisica Nucleare in Italy, the Ministry of Education, Culture, Sports, Science and Technology (MEXT), High Energy Accelerator Research Organization (KEK) and Japan Aerospace Exploration Agency (JAXA) in Japan, and the K. A. Wallenberg Foundation, the Swedish Research Council and the Swedish National Space Board in Sweden.

Additional support for science analysis during the operations phase is gratefully acknowledged from the Istituto Nazionale di Astrofisica in Italy and the Centre National d'Études Spatiales in France. This work performed in part under DOE Contract DE-AC02-76SF00515.

This work made extensive use of the ATNF pulsar catalog¹⁷ (Manchester et al. 2005). This research has made use of the NASA/IPAC Extragalactic Database (NED) which is operated by the Jet Propulsion Laboratory, California Institute of Technology, under contract with the National Aeronautics and Space Administration, and of archival data, software and online services provided by the ASI Science Data Center (ASDC) operated by the Italian Space Agency.

This research has made use of Aladin¹⁸, TOPCAT¹⁹ and APLpy, an open-source plotting package for Python²⁰. The authors acknowledge the use of HEALPix²¹ (Górski et al. 2005). The extended sources were taken from the Manitoba SNR catalog (Ferrand & Safi-Harb 2012).

Facility: Fermi LAT

REFERENCES

- Abdo, A. A., Ackermann, M., Ajello, M., et al. 2009a, *Astroparticle Physics*, 32, 193, doi: [10.1016/j.astropartphys.2009.08.002](https://doi.org/10.1016/j.astropartphys.2009.08.002)
- . 2009b, *ApJL*, 706, L1, doi: [10.1088/0004-637X/706/1/L1](https://doi.org/10.1088/0004-637X/706/1/L1)
- . 2009c, *ApJS*, 183, 46, doi: [10.1088/0067-0049/183/1/46](https://doi.org/10.1088/0067-0049/183/1/46)
- . 2009d, *ApJL*, 701, L123, doi: [10.1088/0004-637X/701/2/L123](https://doi.org/10.1088/0004-637X/701/2/L123)
- . 2010a, *ApJS*, 188, 405, doi: [10.1088/0067-0049/188/2/405](https://doi.org/10.1088/0067-0049/188/2/405)
- . 2010b, *ApJ*, 712, 459, doi: [10.1088/0004-637X/712/1/459](https://doi.org/10.1088/0004-637X/712/1/459)
- . 2010c, *ApJ*, 713, 146, doi: [10.1088/0004-637X/713/1/146](https://doi.org/10.1088/0004-637X/713/1/146)
- . 2010d, *Science*, 328, 725, doi: [10.1126/science.1184656](https://doi.org/10.1126/science.1184656)
- . 2010e, *ApJ*, 718, 348, doi: [10.1088/0004-637X/718/1/348](https://doi.org/10.1088/0004-637X/718/1/348)
- . 2010f, *Science*, 327, 1103, doi: [10.1126/science.1182787](https://doi.org/10.1126/science.1182787)
- . 2011, *ApJ*, 734, 116, doi: [10.1088/0004-637X/734/2/116](https://doi.org/10.1088/0004-637X/734/2/116)
- Abdo, A. A., Ajello, M., Allafort, A., et al. 2013, *ApJS*, 208, 17, doi: [10.1088/0067-0049/208/2/17](https://doi.org/10.1088/0067-0049/208/2/17)
- Abdo, A. A., et al. 2010g, *ApJL*, 709, L152, doi: [10.1088/2041-8205/709/2/L152](https://doi.org/10.1088/2041-8205/709/2/L152)
- . 2010h, *A&A*, 524, A75+, doi: [10.1051/0004-6361/201014458](https://doi.org/10.1051/0004-6361/201014458)
- . 2010i, *ApJ*, 723, 649, doi: [10.1088/0004-637X/723/1/649](https://doi.org/10.1088/0004-637X/723/1/649)
- Abramowski, A., Aharonian, F., Ait Benkhali, F., et al. 2015, *A&A*, 574, A27, doi: [10.1051/0004-6361/201322694](https://doi.org/10.1051/0004-6361/201322694)
- Acero, F., Ackermann, M., Ajello, M., et al. 2015, *ApJS*, 218, 23, doi: [10.1088/0067-0049/218/2/23](https://doi.org/10.1088/0067-0049/218/2/23)
- . 2016a, *ApJS*, 223, 26, doi: [10.3847/0067-0049/223/2/26](https://doi.org/10.3847/0067-0049/223/2/26)
- . 2016b, *ApJS*, 224, 8, doi: [10.3847/0067-0049/224/1/8](https://doi.org/10.3847/0067-0049/224/1/8)
- . 2016c, *ApJS*, 224, 8, doi: [10.3847/0067-0049/224/1/8](https://doi.org/10.3847/0067-0049/224/1/8)
- ¹⁷ <http://www.atnf.csiro.au/research/pulsar/psrcat>
- ¹⁸ <http://aladin.u-strasbg.fr/>
- ¹⁹ <http://www.star.bristol.ac.uk/~mbt/topcat/>
- ²⁰ <http://aplpy.github.com>
- ²¹ <http://healpix.jpl.nasa.gov/>

- Ackermann, M., Ajello, M., Albert, A., et al. 2012a, *ApJS*, 203, 4, doi: [10.1088/0067-0049/203/1/4](https://doi.org/10.1088/0067-0049/203/1/4)
- 2016a, *PhRvD*, 93, 082001, doi: [10.1103/PhysRevD.93.082001](https://doi.org/10.1103/PhysRevD.93.082001)
- Ackermann, M., Ajello, M., Allafort, A., et al. 2011a, *Science*, 334, 1103
- 2011b, *ApJ*, 743, 171, doi: [10.1088/0004-637X/743/2/171](https://doi.org/10.1088/0004-637X/743/2/171)
- 2012b, *Astroparticle Physics*, 35, 346, doi: [10.1016/j.astropartphys.2011.10.007](https://doi.org/10.1016/j.astropartphys.2011.10.007)
- 2013, *ApJS*, 209, 34, doi: [10.1088/0067-0049/209/2/34](https://doi.org/10.1088/0067-0049/209/2/34)
- Ackermann, M., Ajello, M., Atwood, W. B., et al. 2012c, *ApJ*, 750, 3, doi: [10.1088/0004-637X/750/1/3](https://doi.org/10.1088/0004-637X/750/1/3)
- 2015, *ApJ*, 810, 14, doi: [10.1088/0004-637X/810/1/14](https://doi.org/10.1088/0004-637X/810/1/14)
- 2016b, *ApJS*, 222, 5, doi: [10.3847/0067-0049/222/1/5](https://doi.org/10.3847/0067-0049/222/1/5)
- Ackermann, M., Ajello, M., Baldini, L., et al. 2018, *ApJS*, 237, 32, doi: [10.3847/1538-4365/aacdf7](https://doi.org/10.3847/1538-4365/aacdf7)
- Ackermann, M., Ajello, M., Baldini, L., et al. 2016c, *ApJ*, 826, 1, doi: [10.3847/0004-637X/826/1/1](https://doi.org/10.3847/0004-637X/826/1/1)
- 2017, *ApJ*, 843, 139, doi: [10.3847/1538-4357/aa775a](https://doi.org/10.3847/1538-4357/aa775a)
- Ackermann, M., Albert, A., Atwood, W. B., et al. 2016d, *A&A*, 586, A71, doi: [10.1051/0004-6361/201526920](https://doi.org/10.1051/0004-6361/201526920)
- Ackermann, M., et al. 2011c, *ApJ*, 726, 35, doi: [10.1088/0004-637X/726/1/35](https://doi.org/10.1088/0004-637X/726/1/35)
- Ackermann, M., Ajello, M., Atwood, W. B., et al. 2012d, *ApJ*, 761, 91, doi: [10.1088/0004-637X/761/2/91](https://doi.org/10.1088/0004-637X/761/2/91)
- Aharonian, F., Akhperjanian, A. G., Aye, K.-M., et al. 2005, *A&A*, 439, 1013, doi: [10.1051/0004-6361:20053195](https://doi.org/10.1051/0004-6361:20053195)
- Aharonian, F., Akhperjanian, A. G., Barres de Almeida, U., et al. 2008, *A&A*, 477, 353, doi: [10.1051/0004-6361:20078516](https://doi.org/10.1051/0004-6361:20078516)
- Ajello, M., Allafort, A., Baldini, L., et al. 2012, *ApJ*, 744, 80, doi: [10.1088/0004-637X/744/1/80](https://doi.org/10.1088/0004-637X/744/1/80)
- Ajello, M., Atwood, W. B., Baldini, L., et al. 2017, *ApJS*, 232, 18, doi: [10.3847/1538-4365/aa8221](https://doi.org/10.3847/1538-4365/aa8221)
- Ajello, M., Baldini, L., Barbiellini, G., et al. 2016, *ApJ*, 819, 98, doi: [10.3847/0004-637X/819/2/98](https://doi.org/10.3847/0004-637X/819/2/98)
- Araya, M. 2014, *MNRAS*, 444, 860, doi: [10.1093/mnras/stu1484](https://doi.org/10.1093/mnras/stu1484)
- Araya, M. 2017, *ApJ*, 843, 12, doi: [10.3847/1538-4357/aa7261](https://doi.org/10.3847/1538-4357/aa7261)
- Araya, M. 2018a, *MNRAS*, 474, 102, doi: [10.1093/mnras/stx2779](https://doi.org/10.1093/mnras/stx2779)
- 2018b, *ApJ*, 859, 69, doi: [10.3847/1538-4357/aabd7e](https://doi.org/10.3847/1538-4357/aabd7e)
- Arsioli, B., & Polenta, G. 2018, *Astron. Astrophys.*, 616, A20, doi: [10.1051/0004-6361/201832786](https://doi.org/10.1051/0004-6361/201832786)
- Atwood, W., Albert, A., Baldini, L., et al. 2013, *ArXiv:1303.3514*, <https://arxiv.org/abs/1303.3514>
- Atwood, W. B., Abdo, A. A., Ackermann, M., et al. 2009, *ApJ*, 697, 1071, doi: [10.1088/0004-637X/697/2/1071](https://doi.org/10.1088/0004-637X/697/2/1071)
- Ballet, J., et al. 2015, in *ICRC*, Vol. 34, ICRC 2015, ed. A. S. Borisov et al., 848
- Bird, A. J., Bazzano, A., Malizia, A., et al. 2016, *ApJS*, 223, 15, doi: [10.3847/0067-0049/223/1/15](https://doi.org/10.3847/0067-0049/223/1/15)
- Bregeon, J., Charles, E., & Wood, M. 2013, *ArXiv:1304.5456*, <https://arxiv.org/abs/1304.5456>
- Bruel, P., Burnett, T. H., Digel, S. W., et al. 2018, *arXiv:1810.11394*, <https://arxiv.org/abs/1810.11394>
- Buehler, R., Scargle, J. D., Blandford, R. D., et al. 2012, *ApJ*, 749, 26, doi: [10.1088/0004-637X/749/1/26](https://doi.org/10.1088/0004-637X/749/1/26)
- Capetti, A., Massaro, F., & Baldi, R. D. 2017a, *A&A*, 598, A49, doi: [10.1051/0004-6361/201629287](https://doi.org/10.1051/0004-6361/201629287)
- 2017b, *A&A*, 601, A81, doi: [10.1051/0004-6361/201630247](https://doi.org/10.1051/0004-6361/201630247)
- Caputo, R., Buckley, M. R., Martin, P., et al. 2016, *PhRvD*, 93, 062004, doi: [10.1103/PhysRevD.93.062004](https://doi.org/10.1103/PhysRevD.93.062004)
- Casandjian, J.-M., & Grenier, I. A. 2008, *A&A*, 489, 849, doi: [10.1051/0004-6361:200809685](https://doi.org/10.1051/0004-6361:200809685)
- Chang, Y.-L., Arsioli, B., Giommi, P., & Padovani, P. 2017, *A&A*, 598, A17, doi: [10.1051/0004-6361/201629487](https://doi.org/10.1051/0004-6361/201629487)
- Chaty, S., Fortin, F., & Garcia, F. 2018, in preparation
- Condon, J. J., Cotton, W. D., Greisen, E. W., et al. 1998, *AJ*, 115, 1693, doi: [10.1086/300337](https://doi.org/10.1086/300337)
- Coronado, J., Domnguez, A., & Snchez-Conde, M. A. 2019

- D'Abrusco, R., Massaro, F., Paggi, A., et al. 2014, *ApJS*, 215, 14, doi: [10.1088/0067-0049/215/1/14](https://doi.org/10.1088/0067-0049/215/1/14)
- de Ruiter, H. R., Willis, A. G., & Arp, H. C. 1977, *A&AS*, 28, 211
- Devin, J., Acero, F., Ballet, J., & Schmid, J. 2018, *A&A*, 617, A5, doi: [10.1051/0004-6361/201833008](https://doi.org/10.1051/0004-6361/201833008)
- Ferrand, G., & Safi-Harb, S. 2012, *Advances in Space Research*, 49, 1313, doi: [10.1016/j.asr.2012.02.004](https://doi.org/10.1016/j.asr.2012.02.004)
- Górski, K. M., Hivon, E., Banday, A. J., et al. 2005, *ApJ*, 622, 759, doi: [10.1086/427976](https://doi.org/10.1086/427976)
- Green, D. A. 2014, *Bulletin of the Astronomical Society of India*, 42, 47, <https://arxiv.org/abs/1409.0637>
- Griffin, R. D., Dai, X., & Thompson, T. A. 2016, *ApJL*, 823, L17, doi: [10.3847/2041-8205/823/1/L17](https://doi.org/10.3847/2041-8205/823/1/L17)
- Grondin, M.-H., Funk, S., Lemoine-Goumard, M., et al. 2011, *ApJ*, 738, 42, doi: [10.1088/0004-637X/738/1/42](https://doi.org/10.1088/0004-637X/738/1/42)
- H. E. S. S. Collaboration, Abdalla, H., Abramowski, A., et al. 2018, *A&A*, 612, A6, doi: [10.1051/0004-6361/201629790](https://doi.org/10.1051/0004-6361/201629790)
- Hanabata, Y., Katagiri, H., Hewitt, J. W., et al. 2014, *ApJ*, 786, 145, doi: [10.1088/0004-637X/786/2/145](https://doi.org/10.1088/0004-637X/786/2/145)
- Harris, W. E. 1996, *AJ*, 112, 1487, doi: [10.1086/118116](https://doi.org/10.1086/118116)
- Hartman, R. C., Bertsch, D. L., Bloom, S. D., et al. 1999, *ApJS*, 123, 79, doi: [10.1086/313231](https://doi.org/10.1086/313231)
- Hayashida, M., Stawarz, L., Cheung, C. C., et al. 2013, *ApJ*, 779, 131, doi: [10.1088/0004-637X/779/2/131](https://doi.org/10.1088/0004-637X/779/2/131)
- Healey, S. E., Romani, R. W., Cotter, G., et al. 2008, *ApJS*, 175, 97, doi: [10.1086/523302](https://doi.org/10.1086/523302)
- Healey, S. E., Romani, R. W., Taylor, G. B., et al. 2007, *ApJS*, 171, 61, doi: [10.1086/513742](https://doi.org/10.1086/513742)
- HI4PI Collaboration, Ben Bekhti, N., Flöer, L., et al. 2016, *A&A*, 594, A116, doi: [10.1051/0004-6361/201629178](https://doi.org/10.1051/0004-6361/201629178)
- Hu, F., & Zidek, J. V. 2002, *Canad. J. Statist.*, 30, 347
- Johannesson, G., Orlando, E., & the Fermi-LAT collaboration. 2013, *ArXiv:1307.0197*, <https://arxiv.org/abs/1307.0197>
- Katagiri, H., Tibaldo, L., Ballet, J., et al. 2011, *ApJ*, 741, 44, doi: [10.1088/0004-637X/741/1/44](https://doi.org/10.1088/0004-637X/741/1/44)
- Katagiri, H., Yoshida, K., Ballet, J., et al. 2016a, *ApJ*, 818, 114, doi: [10.3847/0004-637X/818/2/114](https://doi.org/10.3847/0004-637X/818/2/114)
- Katagiri, H., Sugiyama, S., Ackermann, M., et al. 2016b, *ApJ*, 831, 106, doi: [10.3847/0004-637X/831/1/106](https://doi.org/10.3847/0004-637X/831/1/106)
- Katsuta, J., Uchiyama, Y., Tanaka, T., et al. 2012, *ApJ*, 752, 135, doi: [10.1088/0004-637X/752/2/135](https://doi.org/10.1088/0004-637X/752/2/135)
- Kerr, M. 2010, PhD thesis, University of Washington, *ArXiv:1101.6072*, <https://arxiv.org/abs/1101.6072>
- Kuźmicz, A., Jamroz, M., Bronarska, K., Janda-Boczar, K., & Saikia, D. J. 2018, *ApJS*, 238, 9, doi: [10.3847/1538-4365/aad9ff](https://doi.org/10.3847/1538-4365/aad9ff)
- Lande, J., Ackermann, M., Allafort, A., et al. 2012, *ApJ*, 756, 5, doi: [10.1088/0004-637X/756/1/5](https://doi.org/10.1088/0004-637X/756/1/5)
- Li, J., Rea, N., Torres, D. F., & de Oña-Wilhelmi, E. 2017a, *ApJ*, 835, 30, doi: [10.3847/1538-4357/835/1/30](https://doi.org/10.3847/1538-4357/835/1/30)
- Li, J., Torres, D. F., Cheng, K. S., et al. 2017b, *ApJ*, 846, 169, doi: [10.3847/1538-4357/aa7ff7](https://doi.org/10.3847/1538-4357/aa7ff7)
- Liu, Q. Z., van Paradijs, J., & van den Heuvel, E. P. J. 2007, *VizieR Online Data Catalog*, 346, 90807
- Manchester, R. N., Hobbs, G. B., Teoh, A., & Hobbs, M. 2005, *AJ*, 129, 1993, doi: [10.1086/428488](https://doi.org/10.1086/428488)
- Massaro, E., Giommi, P., Leto, C., et al. 2009, *A&A*, 495, 691, doi: [10.1051/0004-6361:200810161](https://doi.org/10.1051/0004-6361:200810161)
- Mattox, J. R., Bertsch, D. L., Chiang, J., et al. 1996, *ApJ*, 461, 396, doi: [10.1086/177068](https://doi.org/10.1086/177068)
- Mattox, J. R., Wagner, S. J., Malkan, M., et al. 1997, *ApJ*, 476, 692, doi: [10.1086/303639](https://doi.org/10.1086/303639)
- Mauch, T., Murphy, T., Buttery, H. J., et al. 2003, *MNRAS*, 342, 1117, doi: [10.1046/j.1365-8711.2003.06605.x](https://doi.org/10.1046/j.1365-8711.2003.06605.x)
- McConnachie, A. W. 2012, *AJ*, 144, 4, doi: [10.1088/0004-6256/144/1/4](https://doi.org/10.1088/0004-6256/144/1/4)
- Mereghetti, S., Palombara, N. L., Tiengo, A., et al. 2011, *ApJ*, 737, 51, doi: [10.1088/0004-637x/737/2/51](https://doi.org/10.1088/0004-637x/737/2/51)
- Murphy, T., Sadler, E. M., Ekers, R. D., et al. 2010, *MNRAS*, 402, 2403, doi: [10.1111/j.1365-2966.2009.15961.x](https://doi.org/10.1111/j.1365-2966.2009.15961.x)
- Napier, P. J., Bagri, D. S., Clark, B. G., et al. 1994, *IEEE Proceedings*, 82, 658

- Nolan, P. L., Abdo, A. A., Ackermann, M., et al. 2012, *ApJS*, 199, 31, doi: [10.1088/0067-0049/199/2/31](https://doi.org/10.1088/0067-0049/199/2/31)
- Oh, K., Koss, M., Markwardt, C. B., et al. 2018, *The Astrophysical Journal Supplement Series*, 235, 4, doi: [10.3847/1538-4365/aaa7fd](https://doi.org/10.3847/1538-4365/aaa7fd)
- Peng, F.-K., Wang, X.-Y., Liu, R.-Y., Tang, Q.-W., & Wang, J.-F. 2016, *ApJL*, 821, L20, doi: [10.3847/2041-8205/821/2/L20](https://doi.org/10.3847/2041-8205/821/2/L20)
- Petrov, L., Mahony, E. K., Edwards, P. G., et al. 2013, *MNRAS*, 432, 1294, doi: [10.1093/mnras/stt550](https://doi.org/10.1093/mnras/stt550)
- Pittori, C., Verrecchia, F., Chen, A. W., et al. 2009, *A&A*, 506, 1563, doi: [10.1051/0004-6361/200911783](https://doi.org/10.1051/0004-6361/200911783)
- Pivato, G., Hewitt, J. W., Tibaldo, L., et al. 2013, *ApJ*, 779, 179, doi: [10.1088/0004-637X/779/2/179](https://doi.org/10.1088/0004-637X/779/2/179)
- Planck Collaboration, Aghanim, N., Ashdown, M., Aumont, J., et al. 2016, *A&A*, 596, A109, doi: [10.1051/0004-6361/201629022](https://doi.org/10.1051/0004-6361/201629022)
- Popov, S. B., Mereghetti, S., Blinnikov, S. I., Kuranov, A. G., & Yungelson, L. R. 2018, *MNRAS*, 474, 2750, doi: [10.1093/mnras/stx2910](https://doi.org/10.1093/mnras/stx2910)
- Porter, T. A., Jóhannesson, G., & Moskalenko, I. V. 2017, *ApJ*, 846, 67, doi: [10.3847/1538-4357/aa844d](https://doi.org/10.3847/1538-4357/aa844d)
- Rakshit, S., Stalin, C. S., Chand, H., & Zhang, X.-G. 2017, *ApJS*, 229, 39, doi: [10.3847/1538-4365/aa6971](https://doi.org/10.3847/1538-4365/aa6971)
- Sanders, D. B., Mazzarella, J. M., Kim, D.-C., Surace, J. A., & Soifer, B. T. 2003, *AJ*, 126, 1607, doi: [10.1086/376841](https://doi.org/10.1086/376841)
- Schinzell, F. K., Petrov, L., Taylor, G. B., & Edwards, P. G. 2017, *ApJ*, 838, 139, doi: [10.3847/1538-4357/aa6439](https://doi.org/10.3847/1538-4357/aa6439)
- Schinzell, F. K., Petrov, L., Taylor, G. B., et al. 2015, *ApJS*, 217, 4, doi: [10.1088/0067-0049/217/1/4](https://doi.org/10.1088/0067-0049/217/1/4)
- Schmidt, K., Priebe, A., & Boller, T. 1993, *Astronomische Nachrichten*, 314, 371
- Shahbaz, T., & Watson, C. A. 2007, *A&A*, 474, 969, doi: [10.1051/0004-6361:20078251](https://doi.org/10.1051/0004-6361:20078251)
- Smith, D. A., Bruel, P., Cognard, I., et al. 2019, *ApJ*, 871, 78, doi: [10.3847/1538-4357/aaf57d](https://doi.org/10.3847/1538-4357/aaf57d)
- Stappers, B. W., Archibald, A. M., Hessels, J. W. T., et al. 2014, *ApJ*, 790, 39, doi: [10.1088/0004-637X/790/1/39](https://doi.org/10.1088/0004-637X/790/1/39)
- Tang, Q.-W., Wang, X.-Y., & Tam, P.-H. T. 2014, *ApJ*, 794, 26, doi: [10.1088/0004-637X/794/1/26](https://doi.org/10.1088/0004-637X/794/1/26)
- Véron-Cetty, M.-P., & Véron, P. 2010, *A&A*, 518, A10, doi: [10.1051/0004-6361/201014188](https://doi.org/10.1051/0004-6361/201014188)
- Voges, W., Aschenbach, B., Boller, T., et al. 1999, *A&A*, 349, 389
- . 2000, *VizieR Online Data Catalog*, 9029
- Yeung, P. K. H., Kong, A. K. H., Tam, P. H. T., et al. 2017, *ApJ*, 837, 69, doi: [10.3847/1538-4357/aa5df1](https://doi.org/10.3847/1538-4357/aa5df1)
- . 2016, *ApJ*, 827, 41, doi: [10.3847/0004-637X/827/1/41](https://doi.org/10.3847/0004-637X/827/1/41)
- Yoast-Hull, T. M., Gallagher, John S., I., Aalto, S., & Varenus, E. 2017, *MNRAS*, 469, L89, doi: [10.1093/mnrasl/slx054](https://doi.org/10.1093/mnrasl/slx054)
- Zanin, R., Fernández-Barral, A., de Oña Wilhelmi, E., et al. 2016, *A&A*, 596, A55, doi: [10.1051/0004-6361/201628917](https://doi.org/10.1051/0004-6361/201628917)
- Zdziarski, A. A., Malyshev, D., Chernyakova, M., & Pooley, G. G. 2017, *MNRAS*, 471, 3657, doi: [10.1093/mnras/stx1846](https://doi.org/10.1093/mnras/stx1846)
- Zhang, P. F., Xin, Y. L., Fu, L., et al. 2016, *MNRAS*, 459, 99, doi: [10.1093/mnras/stw567](https://doi.org/10.1093/mnras/stw567)

APPENDIX

A. WEIGHTED LOG-LIKELIHOOD

In 3FGL we introduced a first attempt at accounting for systematic errors in the maximum likelihood process itself, at the source detection level. It was not used in the source characterization, however, for lack of a suitable framework. The standard way to account for systematic errors (for example in *XSPEC*²²) is to define them as a fraction ϵ of the signal and add them to the statistical errors in quadrature, in a χ^2 formalism. This can be adapted to the maximum likelihood framework by introducing weights $w_i < 1$ (Hu & Zidek 2002) as

$$\log \mathcal{L} = \sum_i w_i (n_i \log M_i - M_i) \quad (\text{A1})$$

where M_i and n_i are the model and observed counts in each bin, and the sum runs over all bins in space and energy. The source significance can then be quantified in the same way, via the Test Statistic $TS = 2 \log(\mathcal{L}/\mathcal{L}_0)$ in which \mathcal{L} and \mathcal{L}_0 are the (weighted) likelihood with and without the source of interest, respectively.

Since the statistical variance in Poisson statistics is the signal itself, a first guess for the weights could be

$$w_i = \frac{M_i}{M_i + (\epsilon M_i)^2} = \frac{1}{1 + \epsilon^2 M_i} \quad (\text{A2})$$

However, that formulation has a serious flaw, which is that it is not stable to rebinning. If one splits the bins in half, then M_i is split in half while ϵ stays the same (it is defined externally). In the limit of very small bins, obviously the weights will all tend to 1 and the $\log \mathcal{L}$ formula will tend to the unweighted one, even though nothing has changed in the underlying data or the model.

The solution we propose, originally presented in Ballet et al. (2015), is to define a suitable integral over energy (E) and space (\mathbf{r}) $N(\mathbf{r}, E)$ which does not depend on binning. M_i in the weight formula is then replaced by $N(\mathbf{r}_i, E_i)$ taken at the event's coordinates. For the integral over space, since the catalog mostly deals with point sources, the logical solution is to integrate the background under the PSF, i.e., convolve the model with the PSF $P(\mathbf{r}, E)$, normalized to 1 at the peak (this is equivalent, for a flat diffuse emission, to multiplying by the PSF solid angle). Note that the model already contains the PSF, so this amounts to applying a double convolution to the sky model.

For the energy integral the choice is less obvious. The source spectrum is not a narrow line, so convolving with the energy dispersion (similar to what is done for space) is not justified. An integral over the full energy range would give the same weight to all energies, which is clearly not what we want (there is no reason to downplay the few high-energy events). The option we adopt here is to start the integration at the current energy.

$$w_i = \frac{1}{1 + \epsilon^2 N(\mathbf{r}_i, E_i)} \quad (\text{A3})$$

$$N(\mathbf{r}_i, E_i) = \int_{E_i}^{E_{\max}} S(\mathbf{r}_i, E) dE \quad (\text{A4})$$

$$S(\mathbf{r}, E) = \frac{dM}{dE}(\mathbf{r}, E) * P(\mathbf{r}, E) \quad (\text{A5})$$

²² <https://heasarc.gsfc.nasa.gov/xanadu/xspec/>

where dM/dE is the differential model. As energy increases, the spectra (in counts) decrease and the LAT PSF gets narrower so the convolution makes S even steeper than dM/dE . As a result, the integral giving N is nearly always dominated by the lowest energies, so the exact upper bound E_{\max} is not critical. The only spectral region where it is important is the very lowest energies (< 100 MeV) where the effective area rises steeply. In order not to penalize the lowest energies too much, we set $E_{\max} = 2E_i$ in Eq A4.

There are two possibilities to define dM/dE . Since the main origin of the systematic error is the diffuse emission, we can restrict dM/dE to the diffuse emission model only (we call the result model-based weights). On the other hand there are also systematic uncertainties on sources due to PSF calibration and our imperfect spectral representation, so another option is to enter the full model (or the data themselves) into dM/dE (we call the result data-based weights). That second choice limits spurious sources next to bright sources. There is of course no reason why the level of systematics ϵ should be the same for the diffuse emission model and the sources, but in practice it is a reasonable approximation.

Another important point, for the procedure to be stable, is that the weights should not change with the model parameters. So dM/dE must be defined beforehand (for example from a previous fit). In this work we use data-based weights computed from the data themselves, with a common ϵ . The data are not as smooth as the model, but this is not a problem in the regime of large counts where weights play a role.

We assume here that ϵ is a true constant (it depends neither on space nor on energy). For a given ϵ the weights are close to 1 at high energy and decrease toward low energy. At a given energy the weights are smallest where the model is largest (in the Galactic ridge). Considering all event types (not what we do in 4FGL), for 8 years and $\epsilon = 3\%$, at 100 MeV the weights are everywhere less than 12%. They reach 50% at high latitude at 250 MeV, and 90% at 500 MeV. In the Galactic ridge, the weights are 0.5% at 100 MeV, 1.5% at 250 MeV, 5% at 500 MeV, 20% at 1 GeV, 60% at 2 GeV and reach 90% at 4.5 GeV.

There remains a specific difficulty, due to the fact that at a given energy we split the data into several components, each corresponding to a particular event type (with a different PSF). Since the systematics play in the same way on all components, the weights must be computed globally (i.e., weights must be lower when using PSF2 and PSF3 events than when using PSF3 alone). On the other hand, the resulting uncertainties with two components should be smaller than those with a single component (adding a second one adds information). In this work, we started by computing weights w_k individually for each component k (the dependence on E and \mathbf{r} is left implicit). Then we assumed that the final weights are simply proportional to the original ones, with a factor $\alpha < 1$ (α depends on E and \mathbf{r} as well). A reasonable solution is then

$$N_{\min} = \min_k N_k \quad (\text{A6})$$

$$K_{\text{tot}} = \sum_k \left(\frac{N_{\min}}{N_k} \right)^2 \quad (\text{A7})$$

$$\alpha = \frac{1 + \epsilon^2 N_{\min}}{1 + \epsilon^2 N_{\min} K_{\text{tot}}} \quad (\text{A8})$$

$$w_k = \frac{\alpha}{1 + \epsilon^2 N_k} \quad (\text{A9})$$

K_{tot} and α are 1 if one component dominates over the others, and K_{tot} is the number of components if they are all similar.

B. DESCRIPTION OF THE FITS VERSION OF THE 4FGL CATALOG

Table 9. LAT 4FGL FITS Format: LAT_Point_Source_Catalog Extension

| Column | Format | Unit | Description |
|-----------------------|--------|--|--|
| Source_Name | 18A | ... | Source name 4FGL JHHMM.m+DDMMa ^a |
| RAJ2000 | E | deg | Right Ascension |
| DEJ2000 | E | deg | Declination |
| GLON | E | deg | Galactic Longitude |
| GLAT | E | deg | Galactic Latitude |
| Conf_95_SemiMajor | E | deg | Long radius of error ellipse at 95% confidence |
| Conf_95_SemiMinor | E | deg | Short radius of error ellipse at 95% confidence |
| Conf_95_PosAng | E | deg | Position angle (eastward) of the long axis from celestial North |
| ROI_num | I | ... | RoI number (cross-reference to ROIs extension) |
| Extended_Source_Name | 18A | ... | Cross-reference to the ExtendedSources extension |
| Signif_Avg | E | ... | Source significance in σ units over the 100 MeV to 1 TeV band |
| Pivot_Energy | E | MeV | Energy at which error on differential flux is minimal |
| Flux1000 | E | $\text{cm}^{-2} \text{s}^{-1}$ | Integral photon flux from 1 to 100 GeV |
| Unc_Flux1000 | E | $\text{cm}^{-2} \text{s}^{-1}$ | 1σ error on integral photon flux from 1 to 100 GeV |
| Energy_Flux100 | E | $\text{erg cm}^{-2} \text{s}^{-1}$ | Energy flux from 100 MeV to 100 GeV obtained by spectral fitting |
| Unc_Energy_Flux100 | E | $\text{erg cm}^{-2} \text{s}^{-1}$ | 1σ error on energy flux from 100 MeV to 100 GeV |
| SpectrumType | 18A | ... | Spectral type in the global model (PowerLaw, LogParabola, PLSuperExpCutoff) |
| PL_Flux_Density | E | $\text{cm}^{-2} \text{MeV}^{-1} \text{s}^{-1}$ | Differential flux at Pivot_Energy in PowerLaw fit |
| Unc_PL_Flux_Density | E | $\text{cm}^{-2} \text{MeV}^{-1} \text{s}^{-1}$ | 1σ error on PL_Flux_Density |
| PL_Index | E | ... | Photon index when fitting with PowerLaw |
| Unc_PL_Index | E | ... | 1σ error on PL_Index |
| LP_Flux_Density | E | $\text{cm}^{-2} \text{MeV}^{-1} \text{s}^{-1}$ | Differential flux at Pivot_Energy in LogParabola fit |
| Unc_LP_Flux_Density | E | $\text{cm}^{-2} \text{MeV}^{-1} \text{s}^{-1}$ | 1σ error on LP_Flux_Density |
| LP_Index | E | ... | Photon index at Pivot_Energy (α of Eq. 2) when fitting with LogParabola |
| Unc_LP_Index | E | ... | 1σ error on LP_Index |
| LP_beta | E | ... | Curvature parameter (β of Eq. 2) when fitting with LogParabola |
| Unc_LP_beta | E | ... | 1σ error on LP_beta |
| LP_SigCurv | E | ... | Significance (in σ units) of the fit improvement between PowerLaw and LogParabola. A value greater than 4 indicates significant curvature |
| PLEC_Flux_Density | E | $\text{cm}^{-2} \text{MeV}^{-1} \text{s}^{-1}$ | Differential flux at Pivot_Energy in PLSuperExpCutoff fit |
| Unc_PLEC_Flux_Density | E | $\text{cm}^{-2} \text{MeV}^{-1} \text{s}^{-1}$ | 1σ error on PLEC_Flux_Density |
| PLEC_Index | E | ... | Low-energy photon index (Γ of Eq. 3) when fitting with PLSuperExpCutoff |
| Unc_PLEC_Index | E | ... | 1σ error on PLEC_Index |
| PLEC_Expfactor | E | ... | Exponential factor (a of Eq. 3) when fitting with PLSuperExpCutoff |
| Unc_PLEC_Expfactor | E | ... | 1σ error on PLEC_Expfactor |
| PLEC_Exp_Index | E | ... | Exponential index (b of Eq. 3) when fitting with PLSuperExpCutoff |
| Unc_PLEC_Exp_Index | E | ... | 1σ error on PLEC_Exp_Index |
| PLEC_SigCurv | E | ... | Same as LP_SigCurv for PLSuperExpCutoff model |
| Npred | E | ... | Predicted number of events in the model |
| ASSOC_GAM | 18A | ... | Correspondence to previous γ -ray source catalog ^b |
| TEVCAT_FLAG | A | ... | P if positional association with non-extended source in TeVCat |

Table 9 continued on next page

Table 9 (*continued*)

| Column | Format | Unit | Description |
|-----------------|--------|------|--|
| | | | E if associated with an extended source in TeVCat, N if no TeV association |
| ASSOC_TEV | 24A | ... | Name of likely corresponding TeV source from TeVCat, if any |
| CLASS | 5A | ... | Class designation for associated source; see Table 7 |
| ASSOC1 | 28A | ... | Name of identified or likely associated source |
| ASSOC2 | 26A | ... | Alternate name or indicates whether the source is inside an extended source |
| ASSOC_PROB_BAY | E | ... | Probability of association according to the Bayesian method ^c |
| ASSOC_PROB_LR | E | ... | Probability of association according to the Likelihood Ratio method ^c |
| RA_Counterpart | D | deg | Right Ascension of the counterpart ASSOC1 |
| DEC_Counterpart | D | deg | Declination of the counterpart ASSOC1 |
| Unc_Counterpart | E | deg | 95% precision of the counterpart localization ^d |
| Flags | I | ... | Source flags (binary coding as in Table 5) ^e |

^aThe letter at the end can be **e** (extended source), **i** (for Crab nebula inverse Compton) or **s** (for Crab nebula synchrotron).

^bin the order 3FHL > 3FGL > 2FHL > 1FHL > 2FGL > 1FGL > 0FGL.

^cProbabilities < 0.8 are formally set to 0.

^dFor extended counterparts, this reports their extension radius.

^eEach condition is indicated by one bit among the 16 bits forming **Flags**. The bit is raised (set to 1) in the dubious case, so that sources without any warning sign have **Flags** = 0.

The FITS format version of the early release of the 4FGL catalog has five binary table extensions. The extension **LAT_Point_Source_Catalog_Extension** has all of the information about the sources. Its format is described in Table 9.

The extension **GTI** is a standard Good-Time Interval listing the precise time intervals (start and stop in Mission Elapsed Time) included in the data analysis. The number of intervals is fairly large because on most orbits (~95 min) *Fermi* passes through the South Atlantic Anomaly (SAA), and science data taking is stopped during these times. In addition, data taking is briefly interrupted on each non-SAA-crossing orbit, as *Fermi* crosses the ascending node. Filtering of time intervals with large rocking angles, gamma-ray bursts, solar flares, data gaps, or operation in non-standard configurations introduces some more entries. The GTI is provided for reference and would be useful, e.g., for reconstructing the precise data set that was used for the analysis.

The extension **ExtendedSources** (format unchanged since 2FGL) contains information about the 75 spatially extended sources that are modeled in the 4FGL source list (§ 3.4), including locations and shapes. The extended sources are indicated by an **e** appended to their names in the main table.

The extension **ROIs** contains information about the 1748 RoIs over which the analysis ran. In particular it reports the best-fit diffuse parameters. Its format is very close to that in 3FGL, with one exception. The **RADIUS** column is replaced by **CoreRadius** which reports the radius of the RoI core (in which the sources which belong to the RoI are located). The RoI radius (half-width in binned mode) depends on the component, and is given by the core radius plus **RingWidth**, where the latter is given in the **Components** extension.

The extension **Components** is new to 4FGL. It reports the settings of each individual component (15 in all) whose sum forms the entire data set for the SummedLikelihood approach, as described in Table 2. Its format is given by Table 10.

Table 10. LAT 4FGL FITS Format: Components Extension

| Column | Format | Unit | Description |
|------------|--------|------|--|
| Emin | E | MeV | Lower bound of component's energy interval |
| Emax | E | MeV | Upper bound of component's energy interval |
| ENumBins | I | ... | Number of bins inside energy interval |
| EvType | I | ... | Event type selection for this component |
| ZenithCut | E | deg | Maximum zenith angle for this component |
| RingWidth | E | deg | Difference between RoI radius and core radius |
| PixelSize | E | deg | Pixel size for this component (of exposure map in unbinned mode) |
| BinnedMode | I | ... | 0=Unbinned, 1=Binned |
| Weighted | I | ... | 1 if weights were applied to this component |